MARMARA UNIVERSITY

INSTITUTE FOR GRADUATE STUDIES IN PURE AND APPLIED SCIENCES

CURRENT-DRIVEN GENERATION AND STABILIZATION OF MAGNETIC SKYRMIONS

CANER DEGER

Ph.D. THESIS

Department of Physics

Thesis Supervisor

Assoc.Prof.Ilhan YAVUZ

Thesis Co-advisor

Assoc.Prof.Fikret YILDIZ

ISTANBUL, 2019

MARMARA UNIVERSITY

INSTITUTE FOR GRADUATE STUDIES IN PURE AND APPLIED SCIENCES

CURRENT-DRIVEN GENERATION AND STABILIZATION OF MAGNETIC SKYRMIONS

CANER DEGER
(721214003)

Ph.D. THESIS

Department of Physics

Thesis Supervisor

Assoc.Prof.Ilhan YAVUZ

Thesis Co-advisor

Assoc.Prof.Fikret YILDIZ

ISTANBUL, 2019

MARMARA UNIVERSITY
INSTITUTE FOR GRADUATE STUDIES IN PURE AND APPLIED SCIENCES

Caner DEGER, a Doctor of Philosophy student of Marmara University Institute for Graduate Studies in Pure and Applied Sciences, defended his thesis entitled "**Current-Driven Generation and Stabilization of Magnetic Skyrmions**", on May 13, 2019 and has been found to be satisfactory by the jury members.

Jury Members

Assoc.Prof. İlhan YAVUZ (Advisor)
Marmara University .....

Prof. Dr. Savaş BERBER.....(Jury Member)
Gebze Technical University .....

Assist.Prof. Cengiz OKAY .....(Jury Member)
Marmara University .....

Prof. Dr. Mustafa ÖZDEMİR.....(Jury Member)
Istanbul Technical University .....

Prof. Dr. Zikri ALTUN .....(Jury Member)
Marmara University .....

APPROVAL

Marmara University Institute for Graduate Studies in Pure and Applied Sciences Executive Committee approves that Caner DEGER be granted the degree of PhD in Department of Physics, Physics Program on 22.05.2019 .(Resolution no:2019/11-03)

Director of the Institute
Prof. Dr. Bülent EKİCİ

ACKNOWLEDGEMENT

I would like to use this opportunity to thank to the people who have in many ways supported and helped me during my PhD works.

I would like to acknowledge my thesis co-advisor Assoc.Prof. Fikret YILDIZ for his guidance that helped me in all the time of research life and writing of this thesis. His readinessness to help, for the past ten years, have enabled me educate to be a more talented person and better scientist.

Foremost, I would like to extend my sincere appreciation to my thesis co-advisor Assoc.Prof. Ilhan YAVUZ for the his support of my PhD research, for his motivation, patience and knowledge. This work would not have been possible without him.

My sincere thanks also goes to Can DAVUT, Izzet Parug DURU, Taner KALAYCI and Saba KARAKAS. They were welcoming and helpful, and attained many solutions to challenges.

I also would like to thank TÜBİTAK-BİDEB for 2211 bursary program and Marmara University-BAPKO for the project FEN-C-DRP-150218-0065 throughout my PhD studies.

Last but not the least, I would like to extend my appreciation to my wife, Sinem DEĞER for her love and constant support, for all the late nights and early mornings. I should also like to thank my parents, Seher DEĞER and Sezai DEĞER for their supports and guidance throughout my life.

May, 2019 **Caner DEGER**

TABLE OF CONTENTS

ACKNOWLEDGEMENT……...i

TABLE OF CONTENTS……ii

ÖZET……...iv

ABSTRACT……v

CLAIM FOR ORIGINALITY……vi

SYMBOLS……vii

ABBREVIATIONS……..viii

LIST OF FIGURES……...ix

LIST OF TABLES……...xiv

1. INTRODUCTION……...15

1.1. Magnetic Recording……15

1.2. Magnetic Interactions……...19

1.2.1. Heisenberg Exchange Interaction……...……...19

1.2.2. Dzyaloshinskii-Moriya Interaction……20

1.2.3. Interlayer Exchange Coupling……...21

1.3. Magnetic Anisotropy……22

1.4. Zeeman Energy……24

1.5. Magnetic Skyrmions……24

2. MATERIAL AND METHOD……..29

2.1. Micromagnetic Simulations……..29

2.1.1. Skyrmion Generator……..30

2.1.2. Coupled Layers……..33

2.2. Experimental Methods……..35

2.2.1. Sputtering……..35

2.2.2. Magneto-optic Kerr Effect Measurements……37

2.2.3. Magnetic Force Microscopy……..39

3. RESULTS AND DISCUSSION……..42

3.1.Current-Driven Coherent Generation of Magnetic Skyrmions…….42

3.1.1. Generation Process of Skyrmions…….42

3.1.2. Current Density-Generation frequency relationship…….45

3.1.3. The role of anti-notch dimension……..46

3.1.4. Usage of the Generation in a Racetrack Memory…….50

3.2. Impact of Interlayer Exchange Coupling on Magnetic Skyrmions……..51

3.2.1. Skyrmions in Coupled Layers……...52

3.2.2. Effect of Magnetic Anisotropy……..55

3.2.3. Zero Field Skyrmions……56

3.3. Experimental Results……59

3.3.1. Hysteresis Curves……..59

3.3.2. Magnetic Topography……...66

4. CONCLUSIONS……..69

REFERENCES……72

CURRICULUM VITAE…….76

ÖZET

MANYETİK SKYRMİONLARIN AKIM-SÜRÜMLÜ ÜRETİMİ VE STABİLİZASYONU

Anahtar kelimeler: manyetik skyrmionlar, manyetik ince filmler, mikromanyetik simülasyonlar, saçtırma metodu, manyetik kuvvet mikroskobu.

Spintronik bilgi taşıyıcıları olarak manyetik skyrmionları kullanan yeni nesil mantık ve bellek cihazları, dikkate değer manyetik stabiliteleri, kompakt boyutları ve nano-yollardaki çok düşük maliyetli itilme güçleri sayesinde sıkça incelenmektedir. Skyrmion tabanlı spintronik cihazlar gerçekleştirmek için, skyrmion oluşumunu ve dinamiklerini anlamak esastır. Bu çalışmada, bir anti-çentiği belirli bir genişliğe sahip bir kanala yerleştirerek, eş fazlı manyetik skyrmion üretimi üzerine sistematik bir mikromanyetik simülasyon çalışması gerçekleştirilmiştir. Sürüklenme hızının ve skyrmion üretim frekansının uygulanan spin polarize DC akım yoğunluğuna göre ayarlanabileceği ortaya çıkarıldı. Ayrıca manyetik olmayan bir katman ile ayrılmış iki manyetik katmandan oluşan ince film katlı yapılarda manyetik skyrmion oluşumunu da inceledik. Spin presesyon ve sönüm terimini ilgili tüm katkılarla içeren Landau-Lifshitz-Gilbert denklemi, sayısal olarak mikromanyetik çerçeve içinde çözüldü. Kapsamlı sistematik hesaplamalar sayesinde, skyrmion boyutunun dış manyetik alanın yanı sıra tabakalar arası değiş-tokuş etkileşmesi tarafından da kontrol edilebildiği gösterilmiştir. Tabakalar arası değiş-tokuş etkileşmesi ile ayarlanabilen katmanların z yönündeki mıknatıslanma bileşeni, skyrmion çapını kuvvetle etkilemiştir. Manyetik alanın yokluğunda skyrmion fazı, antiferromanyetik veya ferromanyetik olan her iki etkileşme türü için sarmal faz ile birlikte gözlenmiştir. Sıfır alan skyrmionlarının boyutları da etkileşim ile kontrol edilebilmiştir. Sonuçlarımız ve öngülerimizin, skyrmionların bilgi taşıyıcı olarak kullanıldığı skyrmion tabanlı cihazlar için rasyonel bir temel sağlamasını ve bu alandaki gelecek tartışmaları etkilemesini bekliyoruz.

Mayıs, 2019 **Caner DEĞER**

ABSTRACT

CURRENT-DRIVEN GENERATION AND STABILIZATION OF MAGNETIC SKYRMIONS

Keywords: magnetic skyrmions, magnetic thin films, micromagnetic simulations, sputtering, magnetic force microscopy.

The next-generation logic and memory devices using magnetic skyrmions as spintronic information carriers are frequently studied, thanks to their magnetic stability, compact size and low-cost driving forces within nanotracks. In order to realize skyrmion-based spintronic devices, understanding the skyrmion generation and their dynamics are essential. In this study, we have carried out a systematic micromagnetic simulation study on coherent magnetic skyrmion generation in which we theoretically engineered nanotracks by embedding an anti-notch to a channel of certain width. We found that the drift velocity and the skyrmion generation frequency can be tailored by the applied spin-polarized DC current density. We also study the magnetic skyrmion formation in thin-film stacks, are composed of a non-magnetic spacer seperates two magnetic layers. The Landau-Lifshitz-Gilbert equation, including the damping term and the spin precession term with all relevant contributions, is numerically solved within the micromagnetic framework. Through extensive systematic calculations, we find that skyrmion size can be controlled by the interlayer exchange coupling, as well as the external magnetic field. z-component of the layer's magnetization, which can be tailored by the coupling, strongly affects the skyrmion diameter. The skyrmion phase coexists with the helical phase for both types of coupling, being antiferromagnetic or ferromagnetic, in the absence of the magnetic field. The size of the skyrmions at zero field can also be controlled by the interaction. We anticipate that our predictions provide rational basis for devices employ skyrmions as efficient carriers of information, and influence future discussions.

May, 2019 **Caner DEGER**

CLAIM FOR ORIGINALITY

CURRENT-DRIVEN GENERATION AND STABILIZATION OF MAGNETIC SKYRMIONS

In addition to the stability of the skyrmions, the generation and their motion along nanostructures must be accomplished to employ magnetic skyrmions as efficient carriers of information. However, topological stability of skyrmions restrains the creation (or annihilation) by a continuous variation in orientations of spins from a uniform ferromagnetic state. Here, for the first time, we propose a novel design for coherent field-free generation of multiple skyrmions, which can efficiently supply continuous logic information in a race-track memory device, with no time-dependent stimulation or/and no external magnetic field.

Controlling the size of the skyrmions is also crucial for advanced skyrmionic applications. For this, most recent studies have focused on understanding both internal effects, such as strength of the magnetic anisotropy, and external effects such as magnetic field or electric current, on skyrmion size. Controlling the skyrmion size without any external effect or any change in properties of each magnetic layer can be carried out via alternative approaches. Here, to the best of our knowledge, we show, for the first time, that skyrmion diameter can be systematically controlled by the RKKY interactions as well as the external magnetic fields.

May, 2019 **Caner DEGER**

SYMBOLS

J : Exchange interaction energy

M : Magnetization

μ_0 : Vacuum permeability

N_{sk} : Skyrmion number

γ : Gyromagnetic ratio

α : Gilbert damping constant

H_{eff} : Effective field

Γ_{st} : Spin torque

μ_B : Bohr magneton

j : Current density

β : Nonadiabatic spin torque parameter

M_S : Saturation magnetization

A : Exchange stiffness

D : DMI constant

K : Anisotropy constant

w : Width

l : Length

nm : Nanometer

P : Polarization

Å : Angström

f : Frequency

μ : Mobility

B_{ext} : External magnetic field

ABBREVIATIONS

NMR : Nuclear Magnetic Resonance

HDD : Hard Disk Drive

AFM : Atomic Force Microscopy

MFM : Magnetic Force Microscopy

RAM : Random Access Memory

DMI : Dzyaloshinskii Moriya Interaction

RKKY : Ruderman-Kittel-Kasuya-Yosida

PMA : Perpendicular Magnetic Anisotropy

LLG : Landau-Lifshitz-Gilbert

CIP : Current in-plane

MOKE : Magneto-optic Kerr Effect

DC : Direct Current

DW : Domain Wall

ICIS : Interlayer Coupling Induced Skyrmions

LIST OF FIGURES

PAGE

Figure 1.1 Limestone tablet engraved with pictographic writing…….……..16

Figure 1.2 Components of a typical HDD used in personal computers…….17

Figure 1.3 Atomic Force Microscopy (AFM) and Magnetic Force Microscopy (MFM) images of a HDD platter…….…….17

Figure 1.4 The racetrack memory……...…18

Figure 1.5 Schematic representation of the interfacial DMI for two neighboring spin, S_i and S_j, via an atom has large spin-orbit coupling……21

Figure 1.6 The oscillation periods estimated by the RKKY theory for metals and those measured experimentally…….……...…….22

Figure 1.7 Spin-lattice-orbit interactions……23

Figure 1.8 Spatial configuration of spin construct a skyrmion……...25

Figure 1.9 Spatial magnetization of a skyrmion with a winding number of 1……...26

Figure 1.10 Spatial magnetizations (2D) of depicting states which is not allowed due to the energy consideration in **(a)** and **(b)** with a side view of a skyrmion in **(c)**……27

Figure 1.11 Skyrmion structures with different helicities (γ) and skyrmion numbers (*m*), where the arrows correspond to the direction of the in-plane spin component……...27

Figure 2.1 The design of the magnetic skyrmion generator……...32

Figure 2.2 (left) Schematic representation of the variation of long-range RKKY exchange interaction strength as a function of non-magnetic (NM) spacer thickness…34

Figure 2.3 Diagram of the sputtering process…….36

Figure 2.4 Schematic representation of Si/Pt/Co/Cu/Pt and Si/Pt/$[Co/Cu/Pt]_5$ multilayers structures……...36

Figure 2.5 Gebze Technical University – Thin film growth and characterization system …….37

Figure 2.6 The Kerr effect……..38

Figure 2.7 Measurement geometry of MOKE……38

Figure 2.8 Schematic representation of Magneto-optic Kerr Effect measurement geometry for polarized incoming laser light……..…….....39

Figure 2.9 The MFM image is taken by monitoring the changes in amplitude and phase……40

Figure 2.10 MFM system in Marmara University Physics Department……...40

Figure 2.11 AFM (left) and MFM (right) measurements performed by our AFM Workshop TT-2……...41

Figure 3.1 Reversible conversion between skyrmion-DW pair and coherent skyrmion generation……43

Figure 3.2 Sustainability of multiple skyrmion generation. The response of multiple skyrmion generation to switching of the current at random moments……45

Figure 3.3 Skyrmion generation with respect to current……46

Figure 3.4 Two different anti-notch which prevent coherent skyrmion generation…...47

Figure 3.5 Dependency of coherent generation process on width and length of the anti-notch……49

Figure 3.6 The matrix chart represents the dependency of multiple skyrmion generation on uniaxial magnetic anisotropy (K_1) and exchange stiffness (A_{ex})……50

Figure 3.7 Writing-reading process in a racetrack by using the proposed skymion generator……..51

Figure 3.8 Spatial magnetization of equilibrium skyrmion lattice phase for non-interacting case (JRKKY =0.0 mJ/m2) under external magnetic field of 750 mT…….53

Figure 3.9 Schematic representation of z-component of magnetization vectors under magnetic field of 250 mT, 750 mT and 1250 mT as indicated by gray vertical dashed lines……..55

Figure 3.10 Spatial magnetizations of individual layers for different anisotropy constants……..56

Figure 3.11 The spatial magnetization of the system without an external magnetic field ……57

Figure 3.12 (a) The skyrmion diameter with respect to the magnetic field is shown for the RKKY coupling of J_{RKKY}=-0.1 and 0.1 mJ/m^2 with green and red lines, respectively. The trend of the decreasing diameter of antiferromagnetic and ferromagnetic coupling is similar. (b) The skyrmion diameter as a function of RKKY coupling under magnetic field of 250 mT and 750 mT. (c) The heat map of the skyrmion diameter versus RKKY coupling and magnetic field in the x and y directions, respectively……59

Figure 3.13 Si(100)/Pt(4nm)/Co(0.6nm)/Cu(0.6nm)/Pt(3.4nm)……60

Figure 3.14 The hysteresis curve of Si(100)/Pt(4nm)/Co(0.6nm)/Cu(0.6nm)/Pt(3.4nm) measured in polar geometry……60

Figure 3.15 Si(100)/Pt(4nm)/Co(0.6nm)/Cu(1.2nm)/Pt(2.8nm)……61

Figure 3.16 The hysteresis curve of Si(100)/Pt(4nm)/Co(0.6nm)/Cu(1.2nm)/Pt(2.8nm) measured in polar geometry……62

Figure 3.17 Si(100)/Pt(4nm)/Co(0.6nm)/Cu(1.8nm)/Pt(2.2nm)……62

Figure 3.18 The hysteresis curve of Si(100)/Pt(4nm)/Co(0.6nm)/Cu(1.2nm)/Pt(2.8nm) measured in polar geometry……63

Figure 3.19 The hysteresis curve of Si(100)/Pt(4nm)/Co(0.6nm)/Cu(1.2nm)/Pt(2.8nm) measured in longitudinal geometry……64

Figure 3.20 Si(100)/Pt(4nm)/$[Co(0.6nm)/Cu(1.8nm)/Pt(2.2nm)]_5$……64

Figure 3.21 The hysteresis curve of Si(100)/Pt(4nm)/[Co(0.6nm)/Cu(1.2nm)/Pt(2.8nm) measured in polar geometry……65

Figure 3.22 The hysteresis curve of Si(100)/Pt(4nm)/[Co(0.6nm)/Cu(1.2nm)/ $Pt(2.8nm)]_5$ measured in longitudinal geometry…….….66

Figure 3.23 MFM image of Si(100)/Pt(4nm)/$[Co(0.6nm)/Cu(1.2nm)/Pt(2.8nm)]_5$ …..67

Figure 3.24 Line profile of the magnetic topography of the thin film multilayer structure Si(100)/Pt(4nm)/$[Co(0.6nm)/Cu(1.2nm)/Pt(2.8nm)]_5$……..68

LIST OF TABLES

PAGE

1. CHAPTER 1 - INTRODUCTION

The word “magnetism” is believed to originate from “Magnesia”, the city in Ionia where a shepherd first noticed that the iron tip of his stick was attracted by a stone. As a one of the oldest branch of natural sciences, magnetism have been utilized to find their location and route their way via compasses, seperate materials via magnets, operate their washing machine via electrical current that produced by magnetic generator and even diagnose their disease via nuclear magnetic resonance (NMR) spectroscopy. Generally, characterizing responses of magnetic materials to external magnetic field and temperature is a main focus of magnetism studies. Quantitave analyses of magnetic materials are mainly based on measuring of their apparent properties such as Curie temperature, coercivity, magnetic anisotropy and saturation magnetization. However, emergent measurement techniques allow to observe magnetic topography of materials, which paves the way for new technologies.

1.1. Magnetic Recording

Recording is a passion of human beings for thousands of years. Limestone Kish tablet is one of the earliest example (3500 BC) of recording from Sumer with pictographic writing[1]. In Modern Era, we still have a lot of thing to record. Actually, ninety percent of the information around the world, has been generated only in the last two years. More than 2.5 billion Gb data is used in a day[2]. During the next year, the amount of digital data produced will exceed 5200 GB for every man, woman and child on Earth[3]. From the Kish tablet to our full HD tablet, mankind have developed lots of hieroglyphs, scripts and writing materials. Recording the data in magnetic materials is one of the best solution to meet the need of today’s world. Valdemar Poulsen invented the magnetic recording more than a century ago and it took about 30 years for magnetic tapes to be successfully commercialized[4, 5]. However, they had not the ability of random access which causes longer access time when compared to punch cards. Then, the RAMAC (random access method of accounting and control) was invented by IBM in 1956, as a first hard disk drive (HDD) with a data storage capacity of 5 MB. More than 60 years later, today, HDDs can storage several tens TB of data in a tenth times smaller area of the RAMAC’s.

Figure 1.1 Limestone tablet scraped with pictographic writing. (Iraq), dated from 3500 BC. Probably, it is the earliest known evidence of recording. [1].

A typical HDD used in personal computers (PCs) can be seen in the figure below with its components[6]. A rotatable read/write arm holds a head which both writes and reads the information on a spinning platter. The capacity of an HDD can be multiplied by stacking several platters. Also, both sides of the platters can be used to store the information. The information is written along lines, named as tracks, which can be seen in Fig. 1.3. The width of a track and the number of bits can be stored along single track determine the capacity of a HDD.

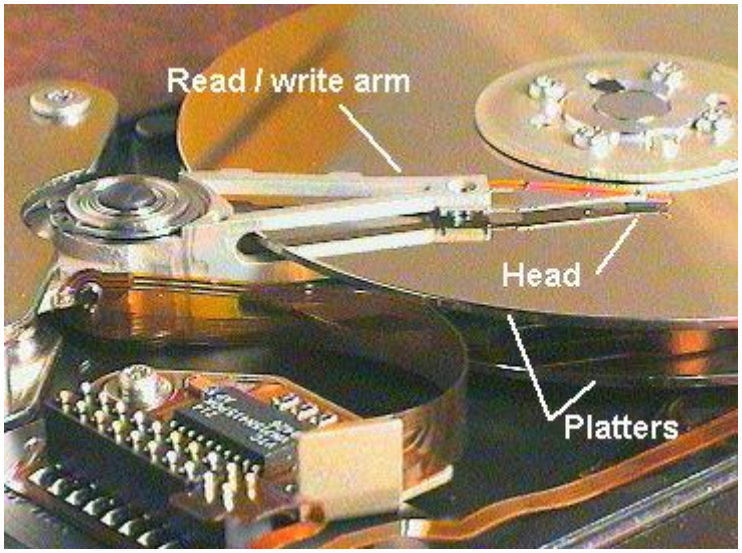

Figure 1.2 Components of a typical HDD used in personal computers[6]

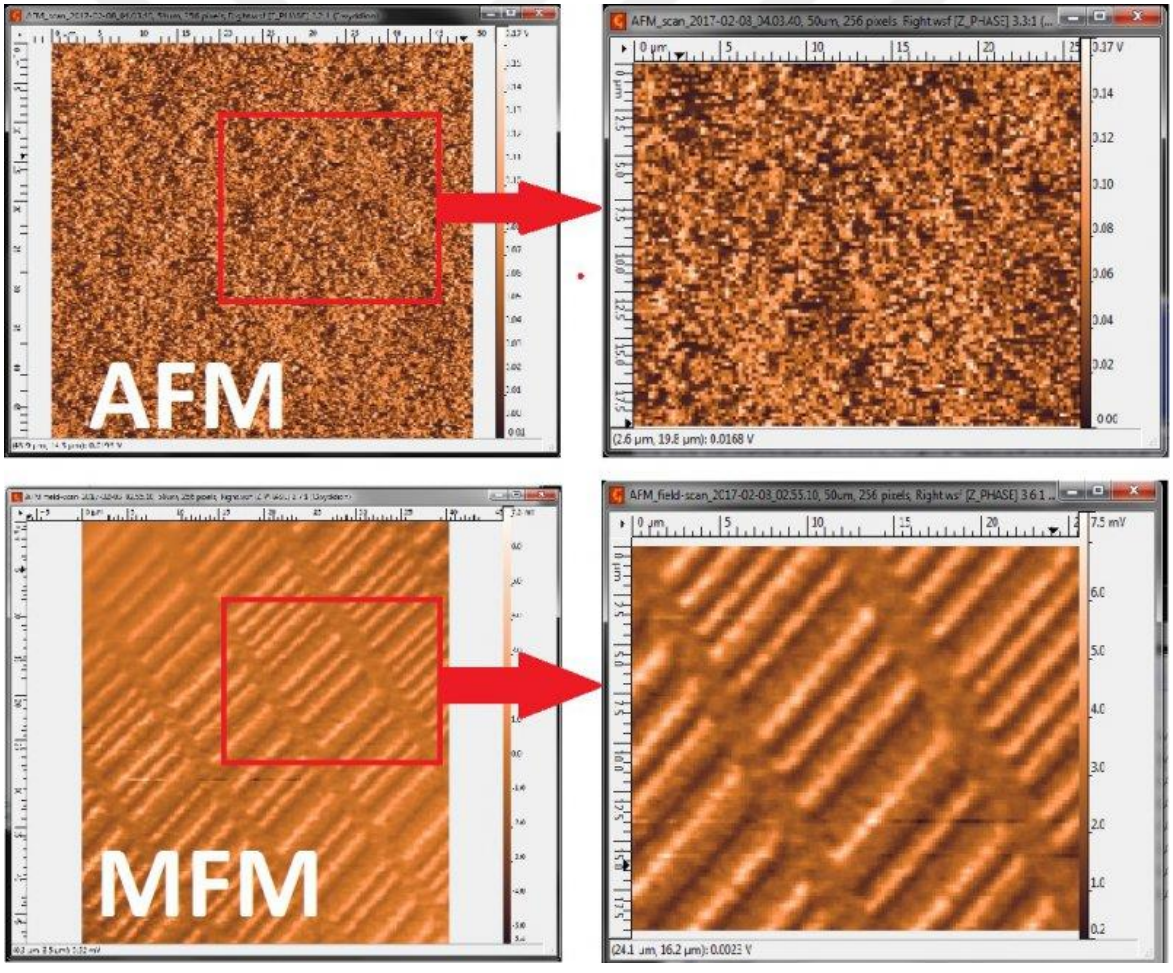

Figure 1.3 Magnetic Force Microscopy and Atomic Force Microscopy images of a HDD platter

The other main concept of storing digital information for computer application, solid-state random access memory (RAM), is very fast and highly reliable when compared to HDD, which is intrinsically slow because of large mass of rotating disk. However, the storage cost for single data bit in an hard disk drive resting a hundred times cheaper than in a solid-state random access memory, approximately. An approach to hybridize the two concept, “Racetrack Memory” promises a single memory storage device with the reliability and high performance of solid-state RAM while the low cost of the HDD[7]. The information is again recorded as magnetic domains, however, in writing/reading process, the domains are propogated by current, instead of rotating disk.

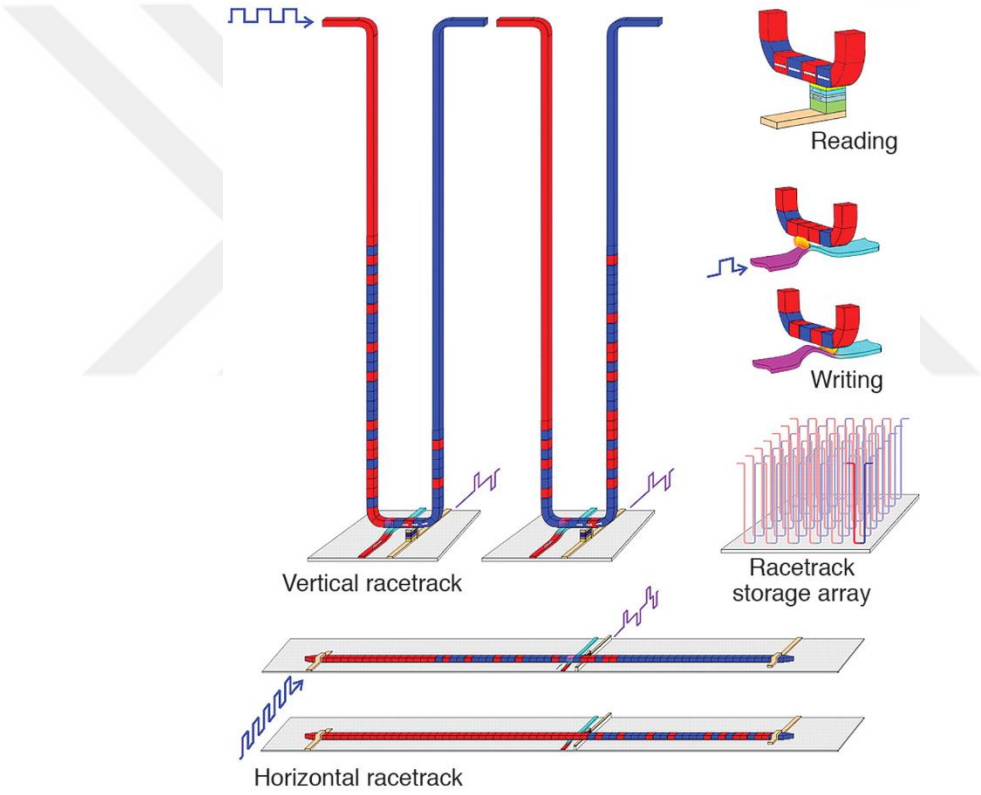

Figure 1.4 The racetrack memory[7].

1.2. Magnetic Interactions

When an experimental physicist needs to measure magnetic properties of a material or structure by ferromagnetic resonance or vibrating sample magnetometer, he puts the sample to an instrument and gets a signal from the whole sample. However, intrinsic magnetic interactions which can only be observed by sophisticated techniques, dominate the magnetic behavior of the structure. In this subsection, three main interactions role in skyrmion formation will be under investigation.

1.2.1. Heisenberg Exchange Interaction

It is simply the interaction between two electrons. It can be stated by a simple case; two hydrogen atoms meet to construct a molecule. At first sight, there are two types of forces; one is attractive forces between protons and electrons, the other is repulsive forces between the two protons and the two electrons. These well-known classical forces can easily be calculated by Coulomb's law. However, since the discovery of the spin phenomena, there is another nonclassical force must be taken into account: exchange interaction. The interaction is caused by the Pauli exclusion principle which states two electrons have the same spin direction can not be exist in the same energy in atom. Thus, if the spins of electrons are parallel, the sum of the all forces is repulsive and a stable molecule can not be formed. However, if the spins are antiparallel, the sum of energies of the atoms is not larger than that of separated state [8]. Then, the two hydrogen atoms can form a stable molecule. The classical Coulomb electrostatic energy can be dominated by the directions of the spins. Thus it can be understood as, the exchange force is basically originated by electrostatic interactions[8]. The exchange energy is one of the important contributions to the total energy of the covalent bond in solids. After the Heisenberg's explanation, it is understood that the exchange interaction also plays an important role in ferromagnetism phonemena.

Heisenberg model defining the energy of neighbouring atoms which have spins $\overrightarrow{S_i}$ and $\overrightarrow{S_j}$ can be given by:

$$H_{Exc} = -J_{ij}\overrightarrow{S_i}\cdot\overrightarrow{S_j} \tag{1.1}$$

where $\overrightarrow{S_i}$ and $\overrightarrow{S_j}$ are the quantum mechanical spins on the atomic sites i and j respectively, and J_{ij} is the energy of this interaction emerging from the probability of the

two electrons exchanging atomic sites. The energy of the interaction between two spins depends on $\overrightarrow{S_i}$ and $\overrightarrow{S_j}$ only through their relative orientation, to be independent of any coordinate system.

1.2.2. Dzyaloshinskii-Moriya Interaction

Antisymmetric exchange, which is also known as the Dzyaloshinskii-Moriya Interaction (DMI), was first postulated by Igor Dzyaloshinskii [9], to construct a model to describe weak ferromagnetism, then modified by Toru Moriya who found the mechanism behind this interaction is partly based on spin-orbit coupling [10]. Qualitatively, it is a contribution to the total magnetic exchange interaction between two neighboring spins which we discussed previous subsection.

A lack of inversion symmetry in interfaces of thin film layers and strong spin-orbit coupling induce the DMI. Inversion symmetry can be splitted in different orientations causing to a different induced DMI [11]. For thin film cases, different magnetizations can induce DMI. The DMI for two neighboring spins can be written as:

$$H_{DM} = -\vec{D}_{ij} \cdot \left(\overrightarrow{S_i} \times \overrightarrow{S_j} \right) \tag{1.2}$$

Here, $\overrightarrow{S_i}$ and $\overrightarrow{S_j}$ are spins of neighbouring atoms and $\vec{D}_{ij}$ is DMI vector. In Fig. 1.5, I represent the schematic explanation of DMI. The DMI occurs at the interface of ferromagnetic thin layer (blue atoms) and non-magnetic layer with a large spin-orbit coupling (dark red atoms) by interplay of $\overrightarrow{S_i}$ and $\overrightarrow{S_j}$. The cross-product in the formulation leads a triangle mechanism which produces DMI vector perpendicular to the triangle. The directions of two neighboring spins tend to be perpendicular to each other for minimizing the DMI energy, which is the reason of calling DMI as antisymmetric exchange.

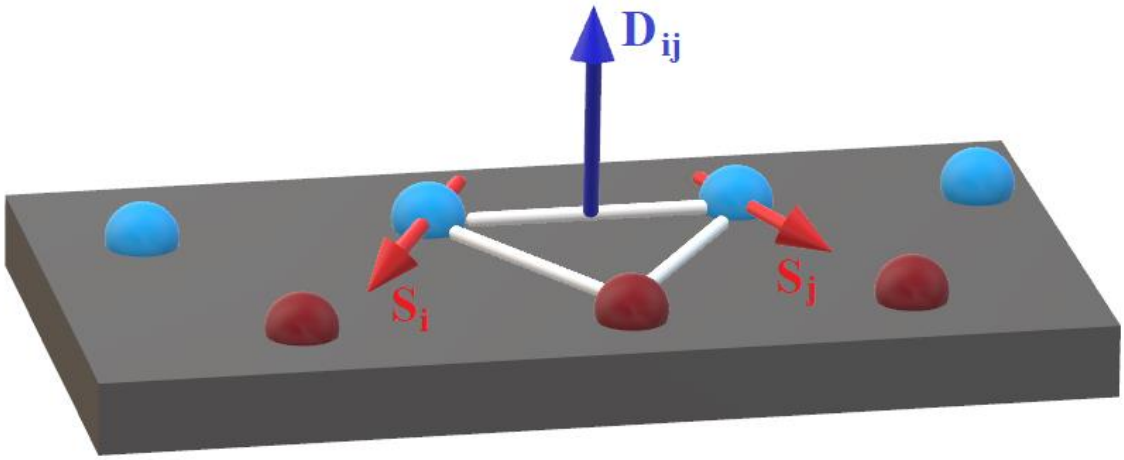

Figure 1.5 Schematic representation of the interfacial DMI for two neighboring spin, S_i and S_j, via an atom has large spin-orbit coupling

1.2.3. Interlayer Exchange Coupling

The magnetizations of two magnetic layer separated by a non-magnetic spacer layer are coupled to each other through the interaction of exchange, via the electrons belonging to the spacer layer. The strentgh and sign (ferromagnetic or antiferromagnetic) of the coupling oscillate by changing spacer layer thickness. This coupling is strongly related to the oscillatory coupling, known as the Ruderman-Kittel-Kasuya-Yosida (RKKY) interaction [12-14], between magnetic impurities in a non-magnetic host [15]. In RKKY interaction, magnetic impurities in a non-magnetic host are coupled to each other by their influence on the electrons in host material. In interlayer exchange coupling, interfaces, as a localized and spin-polarized disturbances, are again coupled to each other by the influence on the electrons in non-magnetic spacer layer. A single interface generates an oscillatory polarization in the non-magnetic spacer. The interface scatters all electrons and an oscillatory probability density occurs for each electron caused by the interference between the incoming and scattered waves. Thus, all states below the Fermi energy form an oscillatory spin density, as a result of spin-up and spin-down electrons scatter differently. This first spin density also arranges the spin density couples to the second interface. Consequently, the interlayer exchange coupling has an oscillatory behavior since the spin density oscillates by varying the spacer layer thickness. The period of the oscillations belonging several noble metals can be seen in the Figure 1.6.

Theory		Experiment	
Spacer	Period(s)	System	Period(s)
Cu(111)	$\Lambda = 4.5$ ML's	Co/Cu/Co	$\Lambda \approx 6$ ML's
		Co/Cu/Co	$\Lambda \approx 5$ ML's
		Fe/Cu/Fe	$\Lambda \approx 6$ ML's
Cu (001)	$\Lambda_1 = 2.6$ ML's $\Lambda_2 = 5.9$ ML's	Co/Cu/Co	$\Lambda \approx 6$ ML's
		Fe/Cu/Fe	$\Lambda \approx 7.5$ ML's
		Co/Cu/Co	$\Lambda_1 \approx 2.6$ ML's $\Lambda_2 \approx 8$ ML's
Au (001)	$\Lambda_1 = 2.6$ ML's $\Lambda_2 = 8.6$ ML's	Fe/Au/Fe	$\Lambda_1 \approx 2$ ML's $\Lambda_2 \approx 7$–8 ML's
Ag (001)	$\Lambda_1 = 2.4$ ML's $\Lambda_2 = 5.6$ ML's	Fe/Ag/Fe	$\Lambda_1 \approx 2.4$ ML's $\Lambda_2 \approx 5.6$ ML's
Cu (110)	$\Lambda_1 = 2.1$ ML's $\Lambda_2 = 2.5$ ML's $\Lambda_3 = 3.3$ ML's $\Lambda_4 = 9.6$ ML's	Co/Cu/Co	$\Lambda \approx 9.8$ ML's
bcc Cu(001)[a]	$\Lambda_1 = 2.2$ ML's $\Lambda_2 = 2.6$ ML's	Fe/Cu/Fe	$\Lambda \approx 2$ ML's

[a]ASW calculation of the bulk Fermi surface of bcc Cu, from Ref. [18].

Figure 1.6 The oscillation periods estimated by the RKKY theory [16] for metals and those measured by experiments [17].

1.3. Magnetic Anisotropy

One of the strongest factor effects on magnetic behavior of materials, magnetic anisotropy, means that the dependency of magnetic properties on measurement geometry. Since the magnetic anisotropy is spontaneously formed in many magnetic materials used for technological applications, a fulfilling knowledge of anisotropy is inevitable for designing novel technologies utilize magnetic materials[18, 19]. There are several kinds of anisotropy including crystal anisotropy, shape anisotropy, stress anisotropy, induced anisotropy and exchange anisotropy [8]. In this subsection and thesis, we will only discuss crystal anisotropy, i.e. magnetocrystalline anisotropy.

Spin-orbit coupling is mainly responsible for the magnetocrystalline anisotropy. Before starting the discussion on the relation between spin-orbit coupling and crystal anisotropy, we should know that orbit-lattice coupling is very strong and orbital magnetic

moments are almost entirely quenched. Thus, the lattice strongly stabilizes the orientations of the orbits [8]. The orbital motion and the spin of each electron are also coupled to each other. Because of the coupling, the spin and orbit of the electron tries to reoriented together in the presence of external magnetic field. However, due to the strong coupling between the orbit and lattice, a resistance against to rotation occurs in not only the orbital motion but also the spin axis. (see Figure 1.7) The energy required to change the orientation of the spin system away from the easy axis, favored direction of the magnetization corresponding minimum energy, of a magnetic domain is just the energy required to overcome the spin-orbit coupling. This energy is defined as the magnetic anisotropy energy. In hexagonal crystals, such as that of Co which acquires to form perpendicular magnetic anisotropy in this thesis, the anisotropy energy, E, is only depended on a single angle, the angle θ between the c axis of the crystal and $\mathbf{M_s}$ vector, which allow us to call this anisotropy as uniaxial. The anisotropy energy can be given by:

$$E = K_0 + K_1 \sin^2\theta + K_2 \sin^4\theta + \ldots \tag{1.3}$$

Here, the constants of K_0, K_1, K_2,, are belonging to a certain structure and represented in J/m^3 (SI) and erg/cm^3 (cgs). The first term, K_0, is independent of the angle and thus it is generally ignored since we are only take into account the differentiation in the energy E when the saturation magnetization vector changes its direction from one direction to another. Also, higher powers of sine of the angle are generally not needed, since it is so small, by resulting the neglection of K_2[8].

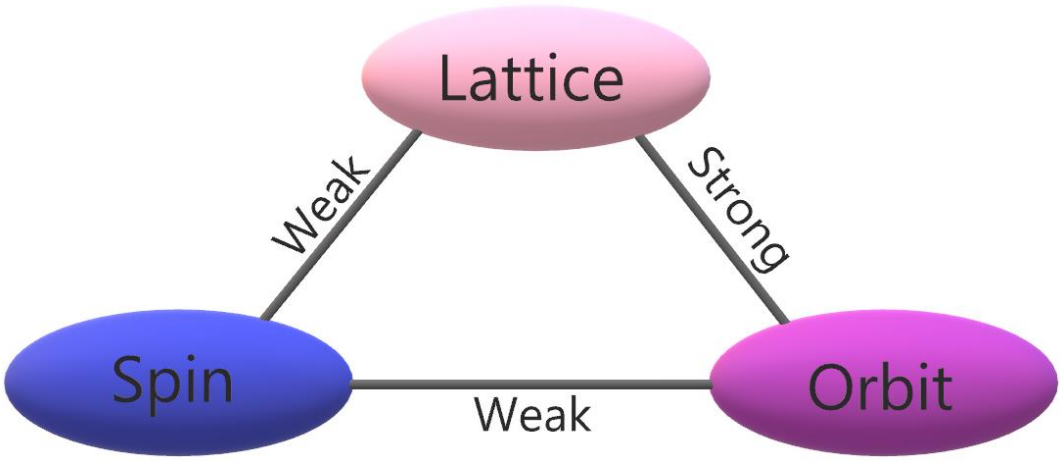

Figure 1.7 Spin-lattice-orbit interactions. The figure adopted from [8].

1.4. Zeeman Energy

Zeeman energy (the external field energy) is the magnetic potential energy of system in an external magnetic field. In other words, the Zeeman energy is the energy of interaction arising from the magnetization vector and any externally applied field. External magnetic fields are produced in different ways, e.g., nearby of magnetic materials, or using an electric current. The applied field energy can be represented by:

$$E_{zeeman} = -\mu_0 \int_V M \cdot H_a dV \quad (1.4)$$

where $\boldsymbol{M}$ is magnetization vector, H_a is the applied magnetic field and μ_0 is the vacuum permeability. The Zeeman energy favors alingment of the magnetization parallel to the applied field.

1.5. Magnetic Skyrmions

Magnetic skyrmions are micron or sub-micron sized particle-like magnetic configurations which have magnetization antiparallel to applied magnetic field at their centre and parallel to the field at their periphery [20, 21]. The potential and diversity of future skyrmionic devices have attracted the interest of numerous investigators. Especially, the next-generation logic and memory devices, which can fundamentally use the skyrmions as the information carrier, are frequently investigated due to its remarkable magnetic stability, extremely compact size and very-low-cost driving force [22-29]. The first observations of Bloch-type magnetic skyrmions have been achieved in B20 materials having a non-centrosymmetric crystalline structure. However, the formation of the skyrmions in B20 compounds such as MnSi and FeCoSi, had required certain conditions, such as low ambient temperature and external magnetic field [23, 30-32]. Later, the attention focused on the ferromagnetic/non-magnetic interfaces having a broken inversion symmetry, which can induce strong Dzyaloshinskii-Moriya interaction (DMI) [9, 10]. Even though the formation of Néel-type skyrmions was achieved at the interfaces exhibit strong DMI, the challenges in the creation of skyrmions were remained, i.e., low temperature conditions and high external magnetic field are still required [33-35]. Finally, Pt/Co/Ta and Co/Pd multilayers with perpendicular magnetic anisotropy (PMA) allowed the first observation of room temperature zero field skyrmions [24, 29, 32]. Further, these systems are considered to be the most suitable candidates for industrial applications since they allow large spin currents resulting in faster skyrmion motions [32].

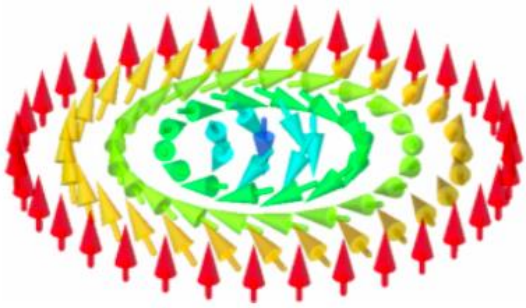

Figure 1.8 Spatial configuration of spin construct a skyrmion [36].

There are several mechanisms playing role in skyrmion formation, including Dzyaloshinskii-Moriya interaction as we discussed above paragraph, can be sorted with the typical skyrmion diameter shown in paranthesis as [11, 37]:

1) Dzyaloshinskii-Moriya interaction, (5-100 nm)
2) Long-ranged magnetic dipolar interactions, (5-100 nm)
3) Frustrated exchange interactions, (~1 nm)
4) Four-spin exchange interactions. (~1 nm)

We already discussed Dzyaloshinskii-Moriya interaction in the subsection 1.2.2 of this thesis. Here, we will not go beyond definition of the other three interaction, which can be found in the literature in detail [11].

The total energy of a spin system can be minimized by a spin configuration of a skyrmion which allow us to call these skyrmion as stable. Also, the spin structure can not be transformed to a trivial structure in the presence of small deformations. Thus, the skyrmion can be defined as topologically protected, with a topological charge (skyrmion number). It is the quantized winding number which counts how many times the configuration wraps around the unit sphere [11]. For a two dimensional spin system, the skyrmion number can be defined as:

$$N_{sk} = \frac{1}{4\pi}\int dx \int dy \; \hat{\Omega}\cdot\left(\frac{\partial}{\partial x}\hat{\Omega}\times\frac{\partial}{\partial y}\hat{\Omega}\right) \qquad (1.5)$$

Here, $\hat{\Omega}$ is the direction of spin at some spatial position.

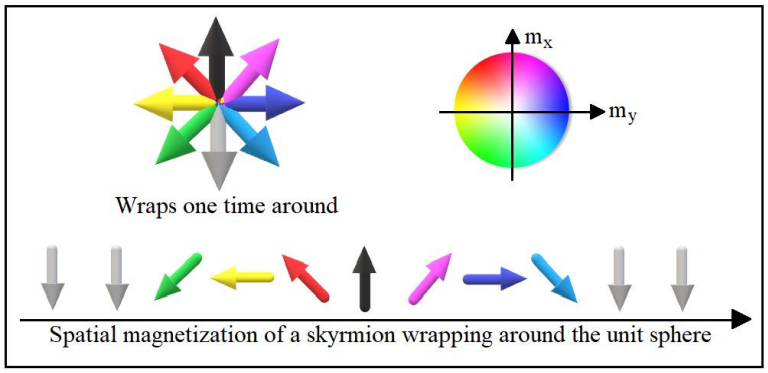

Figure 1.9 Spatial magnetization of a skyrmion with a winding number of 1.

The schematic representation of the topological charge can be seen in Figure 1.9. If the spin structure in the figure is wrapped around a unit sphere, it gives a round which means that the spin structure a winding number of 1. Besides, the skyrmion number can be either +1 or -1 depending on whether the center of the skyrmion is parallel or anti-parallel with the external magnetic field [11].

Spatial magnetization of a spin structure can be dominated by both Dzyaloshinskii-Moriya interaction and exchange interaction. The total energy of the structure can be only minimized by an arrangement minimizing both of the energy of DMI and exchange interaction. As a result of this process, the skyrmion lattice can be formed. Some trivial states which is not allowed based on the energy considerations are shown in Figure 1.10 with a side view of a skyrmion.

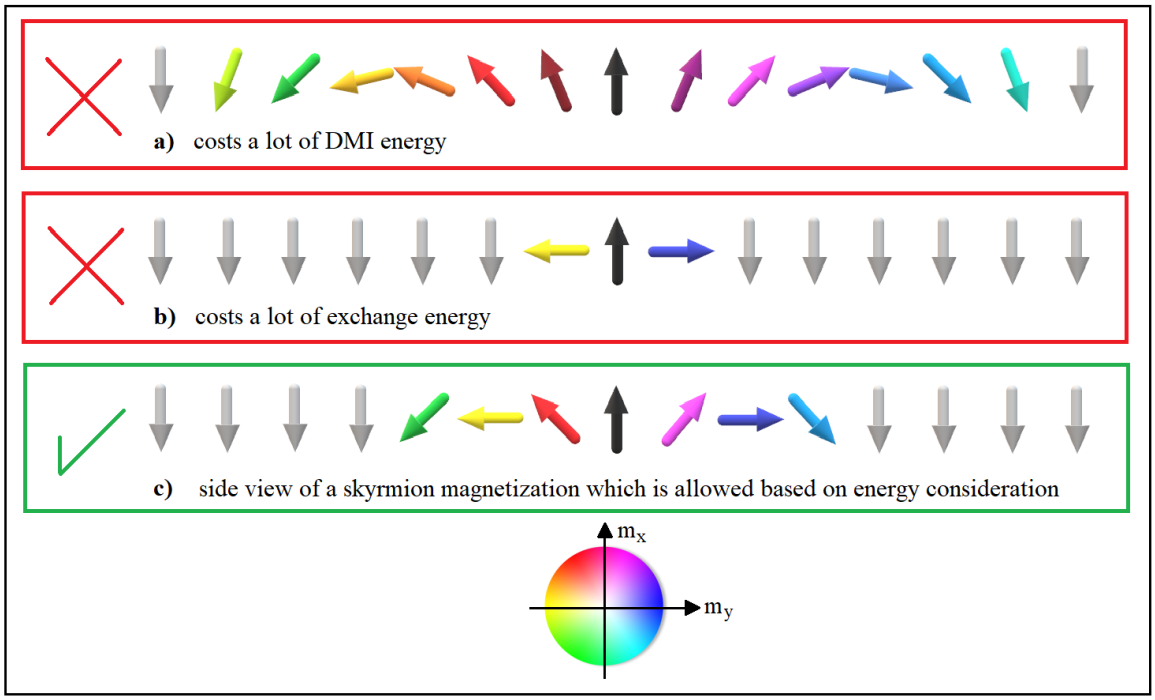

Figure 1.10 Spatial magnetizations (2D) of depicting states which is not allowed due to the energy consideration in **(a)** and **(b)** with a side view of a skyrmion in **(c)**.

Different skyrmion structures can be categorized by their helicity and skyrmion number. The helicity of a skyrmion is depended on the DM interaction exist in the system, which fundamentally related on the direction in which the inversion symmetry is broken in the multilayer thin film structure. Several skyrmion structures with different helicity γ and skyrmion number N_{sk}, can be seen in Figure 1.11 [11, 37].

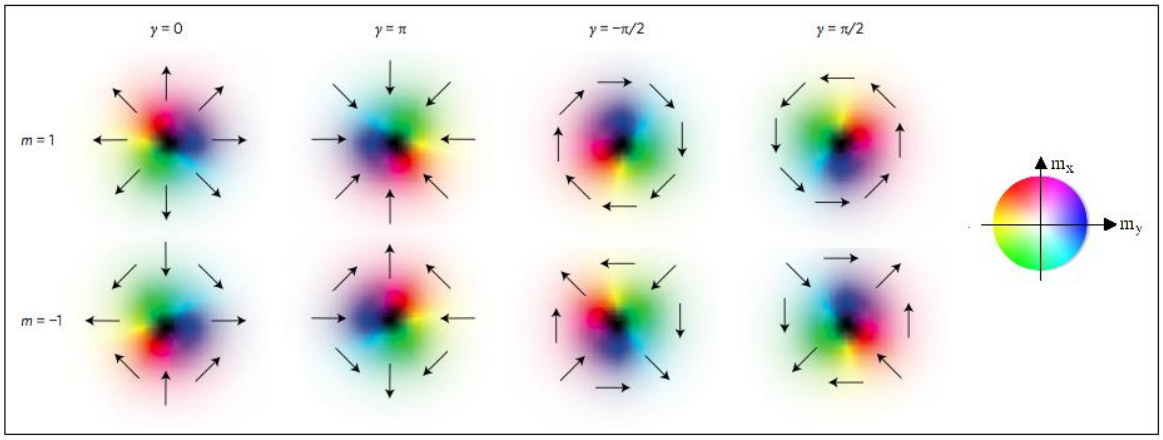

Figure 1.11 Skyrmion structures with different helicities (γ) and skyrmion numbers (N_{sk}), where the arrows correspond to the direction of the in-plane spin component [37].

In this thesis, two novel ideas related to magnetic skyrmions are discussed sequentially in the chapter II (material and method) and chapter III (results and discussion). First, we propose a novel design for coherent field-free generation of multiple

skyrmions, which can efficiently supply continuous logic information in a race-track memory device, with no time-dependent stimulation. This is accomplished by purposely implementing an anti-notch to a nanotrack. Second, we propose a novel approach to control and manipulate the skyrmion size in coupled magnetic thin-film stacks consist of two ferromagnetic layers; a $[Pt/Co]_2$ layer and thicker single layer of Co seperated by a non-magnetic spacer, which allows a long-range Ruderman-Kittel-Kasuya-Yosida (RKKY) exchange coupling between the layers.

2. MATERIAL AND METHOD

Both of the theoretical analyses and experimental studies have been performed to investigate magnetic skyrmions. Even if both of the methods purpose to study the same topic, main differences between theoretical analyses and experiments can exist. Thus, I divide this section to two subsection as micromagnetic simulations and experimental methods.

2.1. Micromagnetic Simulations

Micromagnetic simulations generally deal with the prediction of magnetic behaviors of a spin system under internal and external effects at sub-micrometer length scales. The theory of micromagnetism has allowed the use of calculation methods to estimate magnetic events in the length scale, which is much greater than the interatomic distances. It is a widely accepted model for the identification of magnetic properties of ferromagnetic structures. In 1935 Landau and Lifshitz laid the foundations for this theory, with great contributions from Gilbert, Néel, Bloch, Brown and others. As in other physical systems, this model describes an energy minimization process in which magnetization attempts to reach the lowest energy. In the micromagnetic model, the magnetization dynamics are defined by the time-bound ordinary differential equation called the Landau-Lifshitz-Gilbert (LLG) equation. This equation explains the dynamics of magnetism caused by an effective field. Rapid developments in nanofabrication techniques have further increased interest in computational micromagnetism. In addition, computational magnetism is a popular method since it has little experimental method to characterize the 3D magnetization distribution. Micromagnetic simulations and analyses are two important components of computational micromagnetism. Depending on the nature of the study, one of the two types of micromagnetic simulation (MS) can be used:

1) Static micromagnetic simulations: Static micromagnetic simulations are performed to obtain a spin configuration where the system reaches equilibrium at the end of an estimated simulation time. This may be useful for obtaining a hysteresis curves or for preparing a baseline condition prior to simulating magnetism dynamics. To achieve equilibrium, the Landau-Lifshitz precess can be disabled or the Gilbert damping constant can be increased.

Dynamic micromagnetic simulations: Dynamic micromagnetic simulations are typically used to obtain magnetization dynamics as a function of time. These data are

usually analyzed in different ways for a deeper understanding of the phenomena such as ferromagnetic resonance, spin wave (SW) dynamics, movement of the magnetic domain walls and skyrmions.

Micromagnetic simulation data can be analyzed in two ways: real and inverse zone observations. In real area observations, data is presented in the real space and time zone. This is often used to compare the results of experimental observations and simulation. The inverse region is suitable for obtaining significant results in the frequency or wave vector region with the data that can be transformed into Fourier transform in the time or space region. This is used to obtain modes of magnetization dynamics by exposing the energy density spectrum (ESD).

Computational micromagnetism is an important tool for investigating the internal dynamics of an observed event and for creating a perspective for the next steps, e.g. experimental studies. It is useful for testing, optimization of a design. It provides a way to compare or replace the theoretical model. As with most computational techniques, the methods used in micromagnetism also provide an important area for creating a new model or making new implications for the model studied.

The microscopic parameters of a material such as exchange stiffness (one of the key parameters controlling magnetization reversal in magnetic materials and it serves as characteristic of a ferromagnetic material instead of the exchange integral) and DMI constant determined by experiments and/or first-principle calculations can be input fort he micromagnetic simulations. In this perspective, the simulations can be seen as a bridge between microscopic parameters and macroscopic behaviors of materials. Micromagnetics can deal with both dynamic behavior, such as our proposed skyrmion generator, by solving the time-dependent dynamical equation, and static equilibria, such as our skyrmion size manipulation in coupled layers, by minimizing the magnetic energy.

2.1.1. Skyrmion Generator

The theoretical realization of the proposed coherent skyrmion generation is made possible by micromagnetic simulations based on the Landau-Lifshitz-Gilbert (LLG) equation. The simulations are carried out by employing the micromagnetic software Mumax^3 [38]. The analytic form of the LLG equation, considering separately spin torques Γ_{ST} associated with the current flowing in the film plane (CIP), can be written as [39-41]:

$$\frac{\partial \vec{m}}{\partial t} = -\gamma \vec{m} \times \vec{H}_{eff} + \alpha \vec{m} \times \frac{\partial \vec{m}}{\partial t} + \vec{\Gamma}_{ST}, \tag{2.1}$$

where γ and α are, respectively, the gyromagnetic ratio and the Gilbert damping constant. The first and second terms of the right-hand side of Eq. (1) are the precession and damping terms. We modified the first term and inserted an additional term to the LLG equation, which are Dzyaloshinskii-Moriya interaction term and spin torque term, respectively. The DMI term is included in the system by embedding it in the effective field term (H_{eff}) of the LLG equation. The Dzyaloshinskii-Moriya energy between two interacting sites is given by [9, 10, 42]:

$$E_{ij} = \overrightarrow{D_{ij}} \cdot (\overrightarrow{S_i} \times \overrightarrow{S_j}), \tag{2.2}$$

where $\vec{D}_{ij}$ is the DMI vector which is given by $d\hat{u}_{ij} \times \hat{z}$ [33, 43-45], where $\hat{u}_{ij}$ is the unit vector between sites i and j. Here, $\hat{z}$ represents the unit vector perpendicular to the film plane. We assume a uniform average value along the film thickness by defining a magnetization direction $m(\vec{r})$ at position $\vec{r}$, even though DMI is originated at the interfaces. Thus, the energy originated by DMI, in units of J/m^2, is represented by [42, 46, 47]:

$$E_{DM} = t \int\int D[(m_x \partial_x m_z - m_z \partial_x m_x) + (m_y \partial_y m_z - m_z \partial_y m_y)] d^2\overrightarrow{r}, \tag{2.3}$$

here, D is the continuous effective DM interaction constant across the thin-film.

The other additive term of the LLG equation, spin torque, Γ_{ST}, associated with current flowing in the film plane is expressed in the Zhang-Li form [38, 40, 41]:

$$\overrightarrow{\Gamma}_{st,CIP} = -(\overrightarrow{v_s} \cdot \overrightarrow{\nabla})\overrightarrow{m} + \beta \overrightarrow{m} \times (\overrightarrow{v_s} \cdot \overrightarrow{\nabla})\overrightarrow{m} \tag{2.4}$$

where $\vec{v}_s$ is effective spin-current drift velocity. The magnitude of $\vec{v}_s$ can be written in an explicit form as [40]:

$$|\overrightarrow{v_s}| = -\mu_B p/[eM_s(1 + \beta^2)]j \tag{2.5}$$

where μ_B, j and β are Bohr magneton, current density and nonadiabatic spin torque parameter, respectively.

For micromagnetic simulations, 1-nm-thick cobalt nanotracks with length of 600 nm and width of 10~100 nm on the substrate is considered. The geometry can be seen in Fig. 2.1. The following parameters are adopted to represent intrinsic properties of the layer [20, 25, 29]: M_S = 580 kA/m (saturation magnetization), A = 15 pJ/m (exchange stiffness), D = 3.5 mJ/m^2 (DMI constant), α = 0.3 (Gilbert damping coefficient) and K_1 = 0.8 MJ/m^3, where K_1 represents the constant of the-first order uniaxial magnetic anisotropy, which is an effective anisotropy includes additive terms from the shape and surface anisotropy. The

shape anisotropy originated from the dipole-dipole interactions causes a shift in the constant of uniaxial anisotropy in ultra-thin film cases where the non-local effects are negligible [48, 49]. Our samples are discretized into 600×150×1 unit cells, corresponding to cell size of 1×1×1 nm^3, which is smaller than both the Néel exchange length $\lambda_{Neel} = \sqrt{2A/(\mu_0 M_S^2)}$ = 8.42 nm and the Bloch exchange length $\lambda_{Bloch} = \sqrt{A/K}$ = 4.33 nm.

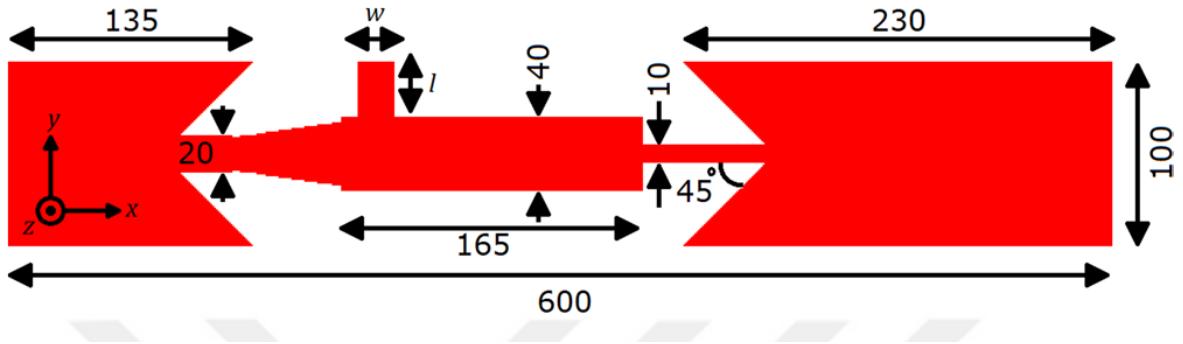

Figure 2.1 The design of the magnetic skyrmion generator. We inject the spin-polarized current into the nanowire with current-in-plane (CIP) geometry. The electrons flow toward +x direction, i.e. the current flows toward −x direction. The current density changes proportionally by the width of the wide or narrow parts of the nanowire. Thus, the current density inside the right chamber is equal to that inside the left chamber. *w* and *l* represent the width and length of the anti-notch, respectively. Here, the units are in nm.

The detailed geometry of the nanotrack is as follows: it consists of three chambers (left, right and central chambers) and are connected by passages. The anti-notch having variable width (w) and length (l) is placed on the left-most section of the central passage. The geometrical parameters of the nanotrack is shown in Fig. 2.1. For our micromagnetic simulations, we first created a skyrmion at the center of left chamber of the nanotrack. Next, we allow the system to relax to a current-free energy minimum state. Then the timer is started and we inject the spin current with a polarization (P) of 1.0 into the nanotrack in the CIP geometry. Subsequently, the current flows toward the left direction so the electrons would flow toward the right. Unless otherwise specified, the non-adiabatic torque coefficient (β) is chosen as to be equal to the damping coefficient, i.e. 0.3, which provides stabilization for the motion of skyrmions along a straight horizontal line through the nanotrack without an additional traverse force.

2.1.2. Coupled Layers

The proposed approach above has been verified by micromagnetic simulations based on the Landau-Lifshitz-Gilbert (LLG) equation. The simulations are carried out by employing the micromagnetic software MuMax^3 [38]. The thin-film stack considered here has non-collinear magnetic structure. The total thickness of $[Pt(2Å)/Co(2Å)]_2$ layer, which will be called as "Pt/Co layer", is 8Å. Here, 2 denotes the layer repetition number. A non-magnetic spacer layer separates the Pt/Co layer from a 22Å-thick single layer of Co, which will be called as "Co layer". The schematic representation of the nanostructure considered in this study is shown in Figure 2.2. The general form of the LLG equation can be written as

$$\frac{\partial \vec{m}}{\partial t} = -\gamma \vec{m} \times \vec{H}_{eff} + \alpha \vec{m} \times \frac{\partial \vec{m}}{\partial t}, \tag{2.6}$$

where γ and α are the gyromagnetic ratio and the Gilbert damping constant, respectively. The first term of Eq. (1) is the precession term while the second is the damping term. For this study, the LLG equation is modified by adding two additional terms, that is Dzyaloshinskii-Moriya interaction term and RKKY interlayer exchange term. Both of the additive interactions are included in the system by embedding them in the effective field term (H_{eff}) of the LLG equation. Since the procedure of DMI calculations mentioned for skyrmion generator in the previous subsection is also valid for this system, I jump to the RKKY calculation.

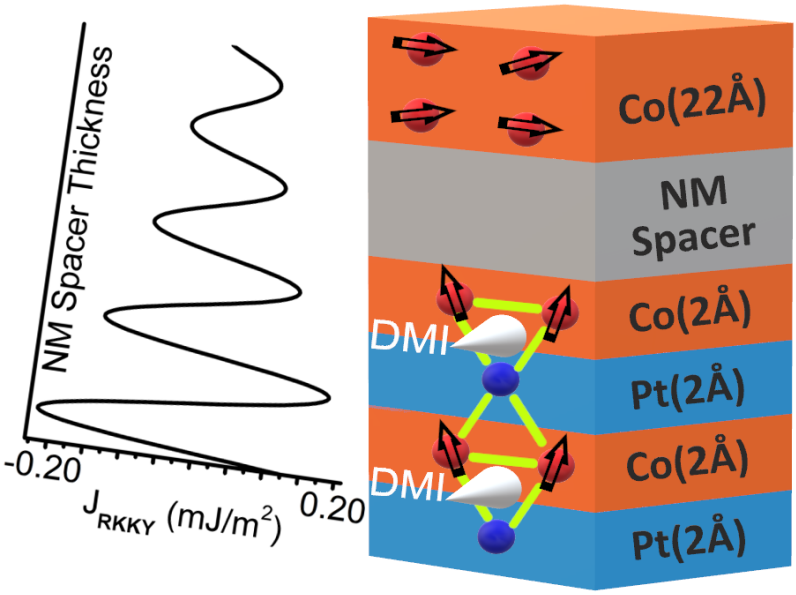

Figure 2.2 (left) Schematic representation of the variation of long-range RKKY exchange interaction strength as a function of non-magnetic (NM) spacer thickness. In our study, the period and damping of the oscillations are arbitrary since the strength and sign of the RKKY interaction is varied explicitly during the simulations. (right) The nanostructure considered in the study. Here, $[Pt(2Å)/Co(2Å)]_2$ layer is assumed as a 'single' magnetic layer with which the simulation parameters corresponds to the desired multilayer.

The long-range RKKY exchange field term is incorporated and rationalized by scaling the exchange coupling between the predefined layers. As mentioned, the nanostructure is composed of a non-magnetic spacer seperates two ferromagnetic layers. We investigate different interlayer exchange interaction values, J_{RKKY}, from -0.2 to 0.2 mJ/m^2, which can occur between the two ferromagnetic layers via thin film spacer having a thickness of several nanometers. The scaling factor (SF) to get the desired long-range exchange interaction is given by SF=(RKKY x cs) / (2 $A_{ex,av}$) where cs is the size of simulated cell along the z direction and $A_{ex,av}$ is the average exchange stiffness of the two coupled layers. We consider two ferromagnetic layers with the dimensions of 200x200 nm^2. Note that, although the specifying elements to construct and simulate the magnetic thin-film stack is not indispensable to reveal the effect of RKKY coupling, we choose the parameters below to compare some of our results with experimental studies. The following parameters are used for the Pt/Co and Co layers: $M_{S(Pt/Co)}$=1.2 x 10^6 A/m (saturation magnetization) [50] and $K_{1(Pt/Co)}$=0.975 x 10^6 J/m^3, where the latter represents the first-order perpendicular uniaxial magnetic anisotropy constant. It is an effective anisotropy

constant includes contributions from the surface anisotropy and the shape anisotropy [48, 49], $M_{S(Co)}$=1.4 x 10^6 A/m [51], $K_{1(Co)}$=1.09 x 10^6 J/m^3 [51], A_{ex}=10 pJ/m (exchange constant), $D_{i(Pt/Co)}$=5 mJ/m^2 [44, 52] and alpha=1.0 (Gilbert damping) [51]. Additionally, RKKY constant (J_{RKKY}) is varied during the simulations in order to map combinations of the parameters above and external magnetic field that can lead to stable skyrmion lattices. We divide our sample into 200 x 200 x 2 unit cells, corresponding to cell size of 1 x 1 x 1 nm^3, which is smaller than both the Néel exchange length $\lambda_{Neel} = \sqrt{2A/(\mu_0 M_S^2)}$ = 3.32 nm and the Bloch exchange length $\lambda_{Bloch} = \sqrt{A/K}$ = 3.20 nm. Periodic boundary conditions in the x and y-directions are imposed in our simulations.

2.2. Experimental Methods

Thin film growth and characterization methods used to investigate magnetic properties of our samples are introduced in this section.

2.2.1. Sputtering

The sputtering method involves a controlled gas to meet the deposition chamber, generally Ar, a deposition chamber, a target material to growth and an electrically energizing cathode to generate a plasma [53]. The target material which is exposed surface of the cathode, is a slab of the material to be growth onto the substrate.

In the growth process, first, the gas atoms lose electrons because of the high induced energy from the cathode inside the plasma, then the atoms evolving to a positively charged ions. The ions, which are begining to move more quickly into the target, are finalizing their movement with sufficient kinetic energy by hitting the target material again, and dislocate molecules or atoms. The sputtered material from the target forms a vapor stream that travels along the vacuum chamber and hits the surface of the slab to grown on it, which we called as coating or "thin film"[53].

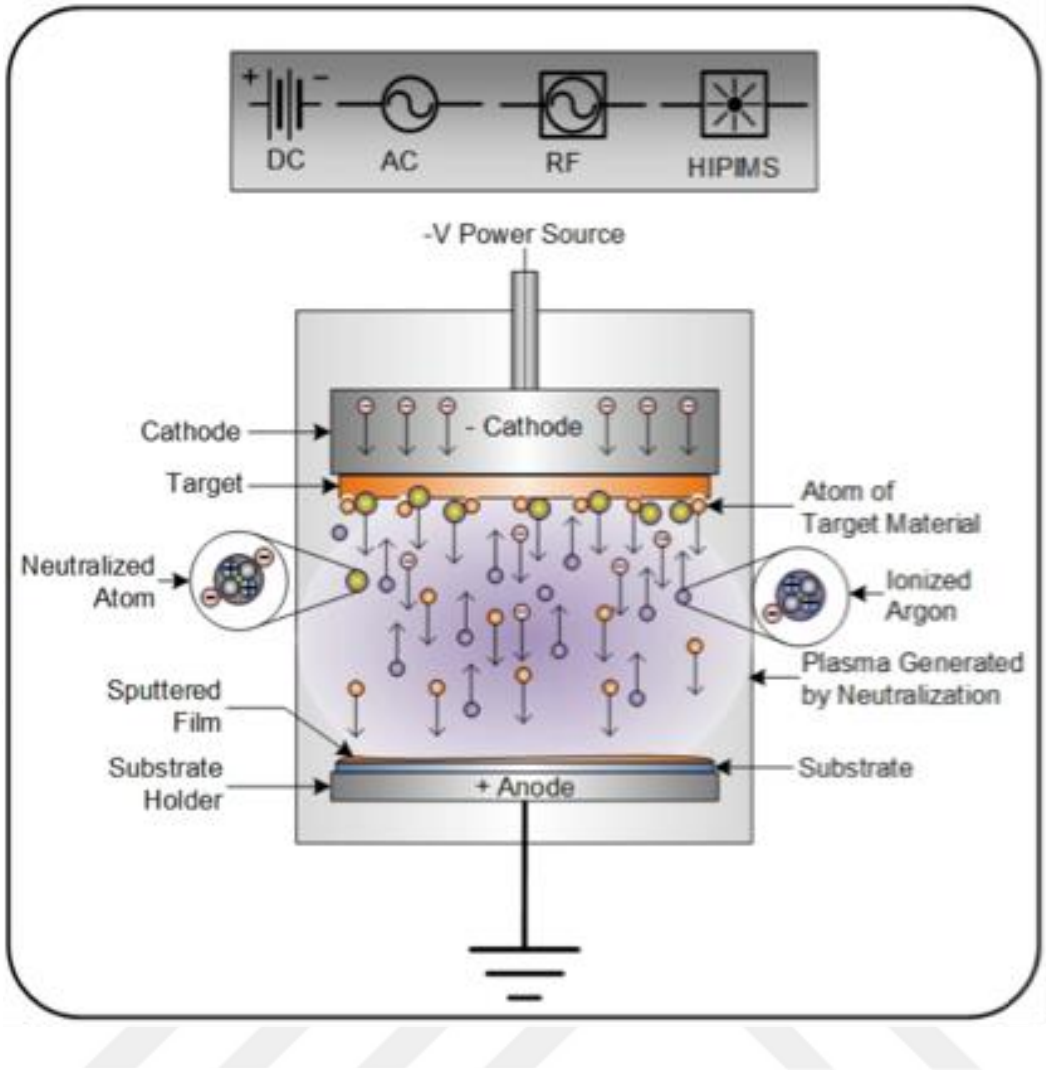

Figure 2.3 Diagram of the sputtering process[51].

The thin film structures represented below are growth by sputtering technique.

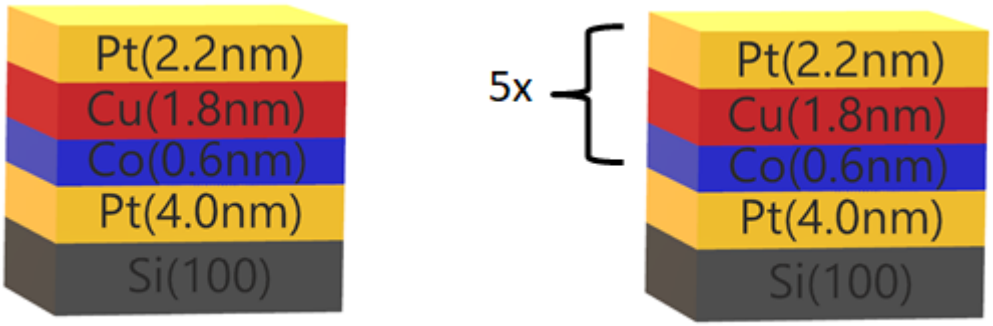

Figure 2.4 Schematic representation of Si/Pt/Co/Cu/Pt and Si/Pt/$[Co/Cu/Pt]_5$ multilayers structures.

Both of the stuctures in Figure 2.4 were grown on Si (100) substrate. All layers were deposited by using magnetron sputtering. At the bottom of the multilayer systems Pt

buffer layer was grown with a thickness of 4 nm in order to induce (111) textures. The base pressure of the sputter chamber is $1x10^{-9}$ mbar and during the deposition Argon (Ar) pressure was $5x10^{-3}$ mbar. Pt and Cu layers were grown by DC generators while Co layers were grown by RF generators. The deposition rates for Pt, Cu and Co layers were 0.772, 1.057 and 0.174 nm/min, respectively.

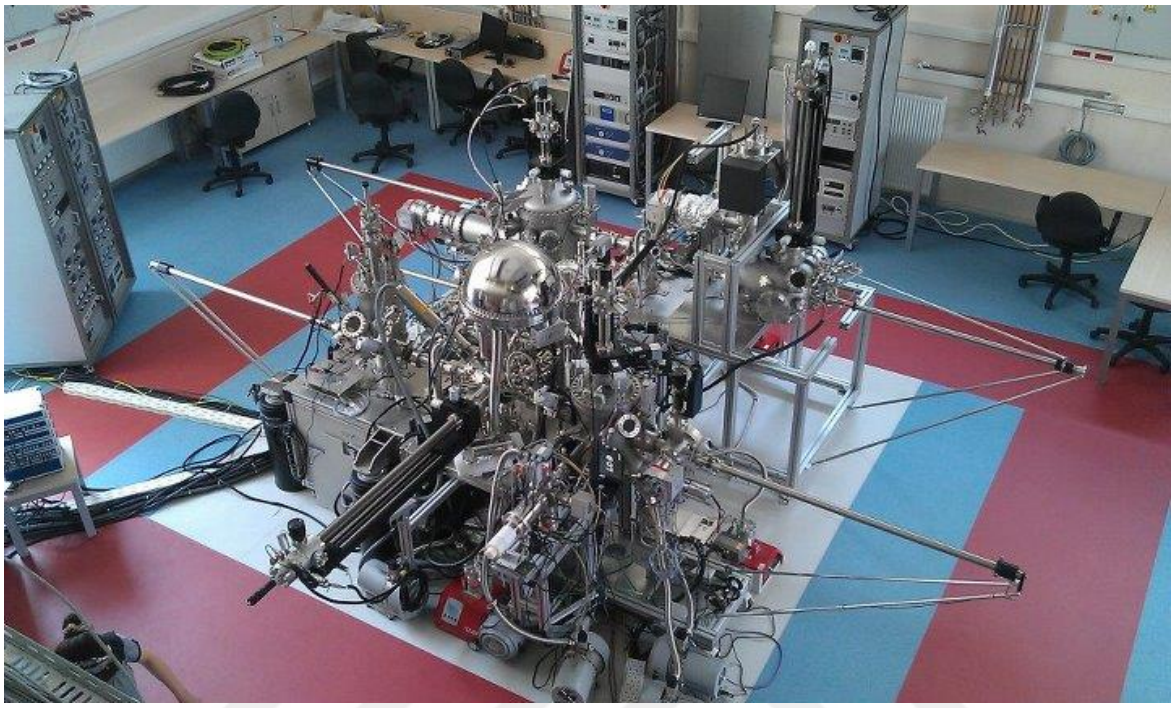

Figure 2.5 Gebze Technical University – Thin film growth and characterization system.

2.2.2. Magneto-optic Kerr Effect Measurements

Magneto-optic Kerr Effect (MOKE) technique is a powerful measurement method to explore surface properties of magnetic materials. MOKE measurement is commonly used as an experimental technique due to its sensitivity, set-up simplicity and local probing nature for different directions of magnetization vector, i.e. polar, longitudinal and transverse. MOKE measurement is based on the change in the polarization of reflected laser beam from the surface of a magnetic material. When polarized light interacts with a magnetic material, its polarization state is influenced (Figure 2.6). The MOKE measurement setup is desinged to detect these small changes in polarization of light can be seen in Fig. 2.7.

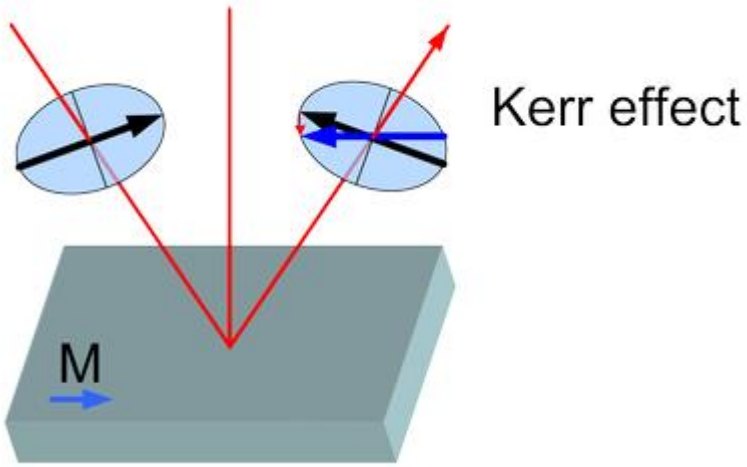

Figure 2.6 The Kerr effect. The figure extracted from

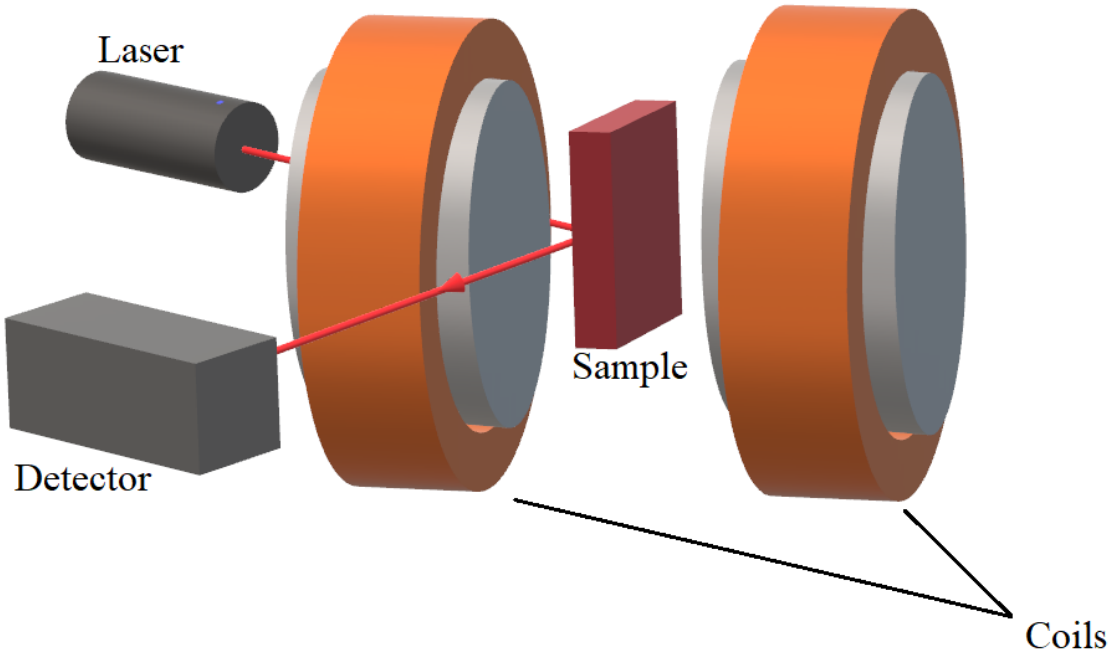

Figure 2.7 Measurement geometry of MOKE

The MOKE measurements of samples were carried out at room temperature and the hysteresis loops were measured for both polar and longitudinal MOKE geometry, which are defined in detail below.

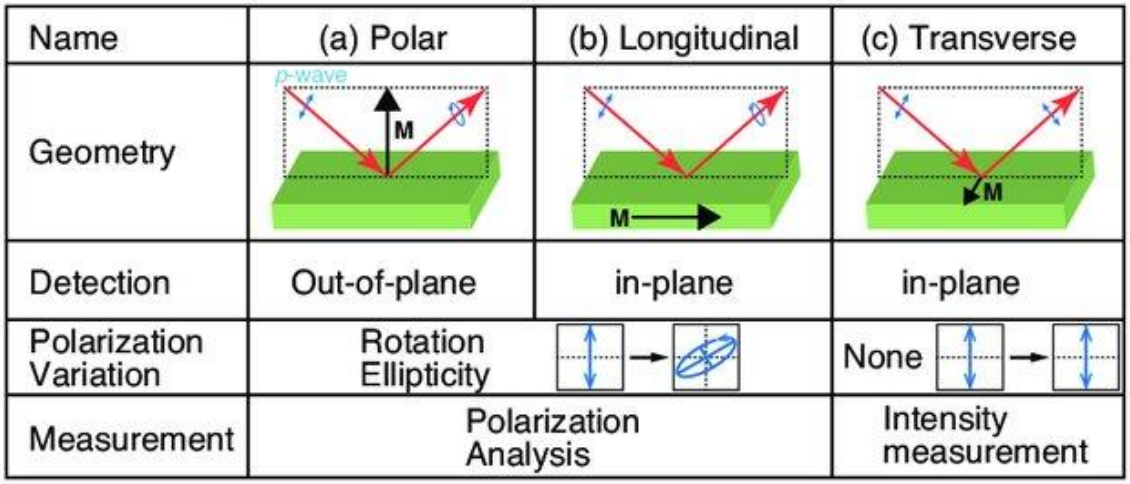

Figure 2.8 Schematic representation of magneto-optic Kerr effect measurement geometry for incoming light has a polarization of p-wave. The dashed line in the skecth of measurement geometries indicates the incoming plane. The row of polarization variation indicates the differentiation in the states of polarization of light which has projection in the plane which inclined parallel to the direction of the move forward of the normal of the light can be seen for both reflected and incoming in right and left, respectively [54].

2.2.3. Magnetic Force Microscopy

Magnetic Force Microscopy (MFM) is a powerful method used to explore surface magnetic fields by using a magnetic probe. The magnetic sample is scanned by a sharp magnetized tip; the tip-sample interactions are measured. Magnetic coating on AFM silicon probes allows to sense magnetic differences along the surface. The most sensitive method for MFM scanning is vibrating mode. In this mode, the probe is oscillating around a fixed distance of 5-200 nm from the sample surface. The cantilever is driven to its resonance frequency, then the laser detects the shifts in frequency.

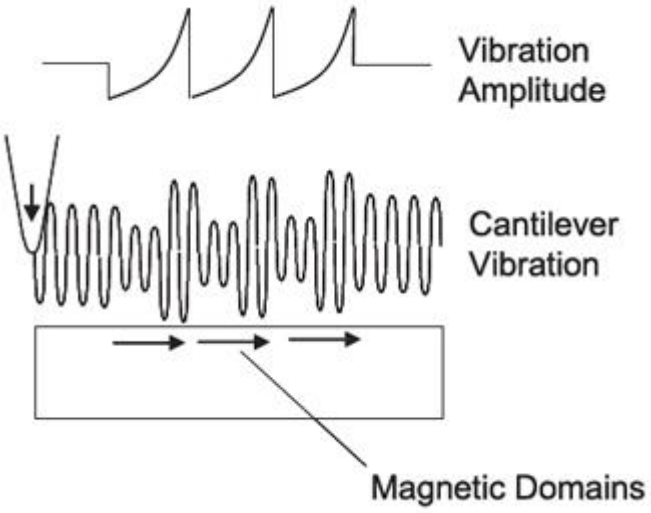

Figure 2.9 The MFM image is generated by monitoring the changes in phase and amplitude.

The resonance frequency can be connected to the natural frequency, by supposing small vibrations to a first-order. The shift in the resonance frequency is caused by changing in the spring constant, which corresponds to the repulsive and attractive forces acting on the cantilever. The resonance frequency of the cantilever decreases for attractive forces.

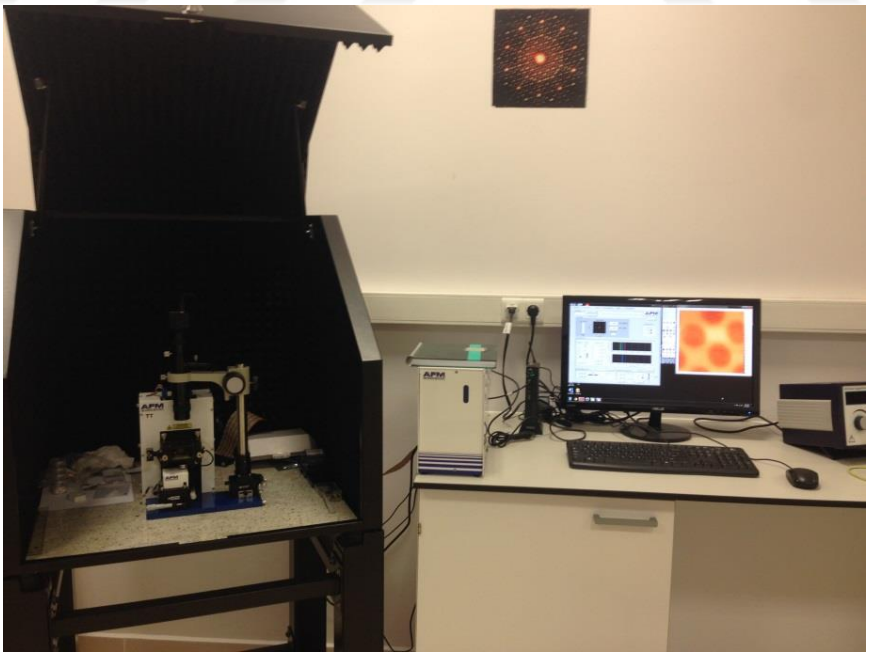

Figure 2.10 MFM system in Marmara University Physics Department

When the cantilever scans the surface of a magnetic sample at close distances (<5 nm), magnetic, van der Waals, electrostatic and atomic forces are sensed all together. A second lifted path of scan is performed to reduce topography artifacts in the MFM image as can be seen in Fig. 2.9[55].

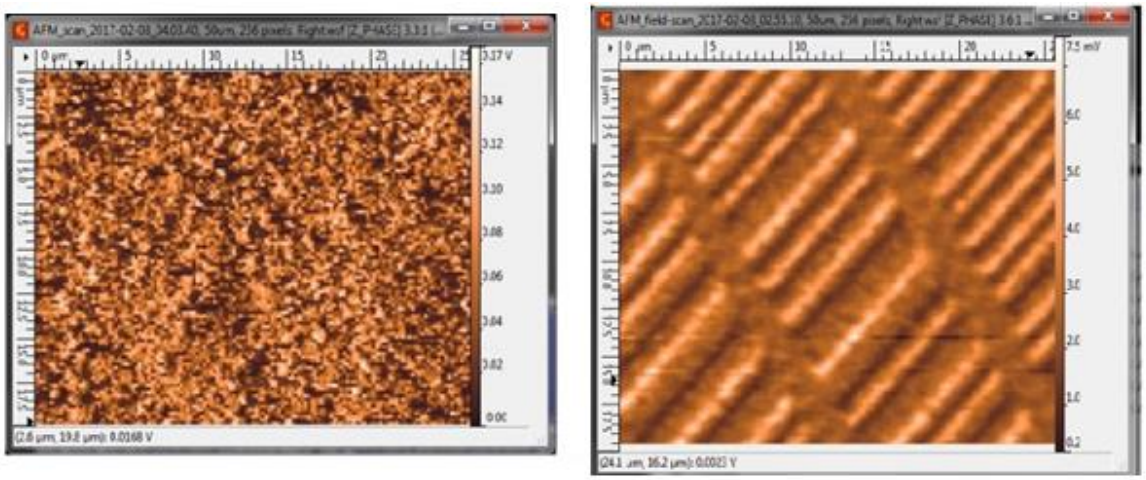

Figure 2.11 AFM (left) and MFM (right) measurements performed by our AFM Workshop TT-2.

3. CHAPTER 3 – RESULTS AND DISCUSSION

This section is divided to three subsection. In first subsection, I introduce a current-driven coherent skyrmion generator. Then, impact of interlayer exchange coupling on magnetic skyrmions will be discussed. In the last subsection, some of our promising experimental results will be represented.

3.1. Current-Driven Coherent Generation of Magnetic Skyrmions

In addition to the stability of the skyrmions, the generation and their motion along nanostructures must be accomplished to use skyrmions as efficient information carriers. However, topological stability of skyrmions restrains the creation (or annihilation) by a continuous variation in spin configuration from a uniform ferromagnetic state [56]. Fortunately, the creation of single skyrmion has been achieved by circulating current [57], ultra-short single optical laser pulses [58] and sub-nanosecond spin-orbit torque pulses [59]. Continuous multiple skyrmion generation has recently been demonstrated by Ma et al. via pulsations of microwave field or spin-polarized current density [60]. Moreover, the demonstration of current-driven transformation from stripe domains to magnetic skyrmion bubbles was recently performed in Ta/CoFeB/TaO trilayers [61].

In this work, using micromagnetic simulations, we propose a novel design for coherent field-free generation of multiple skyrmions, which can efficiently supply continuous logic information in a race-track memory device, with no time-dependent stimulation. This is accomplished by purposely implementing an anti-notch to a nanotrack as shown in Figure 2.1. The spin transfer-induced motion of skyrmions and domain walls in magnetic tracks with an anti-notch is extensively investigated. The spin-polarized DC current-induced skyrmion and domain wall dynamics is found to be strongly dependent on the expanded geometry and boundary effects. We anticipate that our study not only offers a rational geometry for coherent skyrmion generation but also will inspire future considerations about the influence of the enlargement of the nanotracks on current-driven motion of the skyrmions and domain walls.

3.1.1. Generation Process of Skyrmions

To realize the proposed generation process, the conversion between a skyrmion and a domain-wall (DW) pair must be well-understood. Magnetic thin film multilayers with perpendicular magnetic anisotropy can comprise strong DMI at the interfaces, which

consist of a heavy metal layer with high-spin-orbit coupling and a magnetic layer. These multilayers could allow the stabilization of chiral DWs and/or skyrmions [61]. A nanowire geometry which leads to the reversible conversion between a skyrmion and a domain-wall pair is considered in Figure 3.1(a). In this case, skyrmion was first created in the left chamber with an intrinsic diameter of 30 nm, which is determined by the material parameters and confined geometry at t=0. The created skyrmion survives until it is drifted by the applied current toward the end of left chamber having a narrow passage with a width of 20 nm. This narrow passage, normally, does not allow the stabilization of a skyrmion with such diameter, i.e. larger than the width of the passage [62]. Therefore, the skyrmion is transformed into a DW pair at t=0.1 ns. The DW pair propagates rightwards in the central narrow chamber until the DW reaches a 10-nm-sized passage, as shown in Figure 3.1(a) and at t=0.5 ns. Then, DW pair is converted into a skyrmion at t=0.7 ns. This exotic behavior is both theoretically proposed [62] and experimentally observed [61] recently.

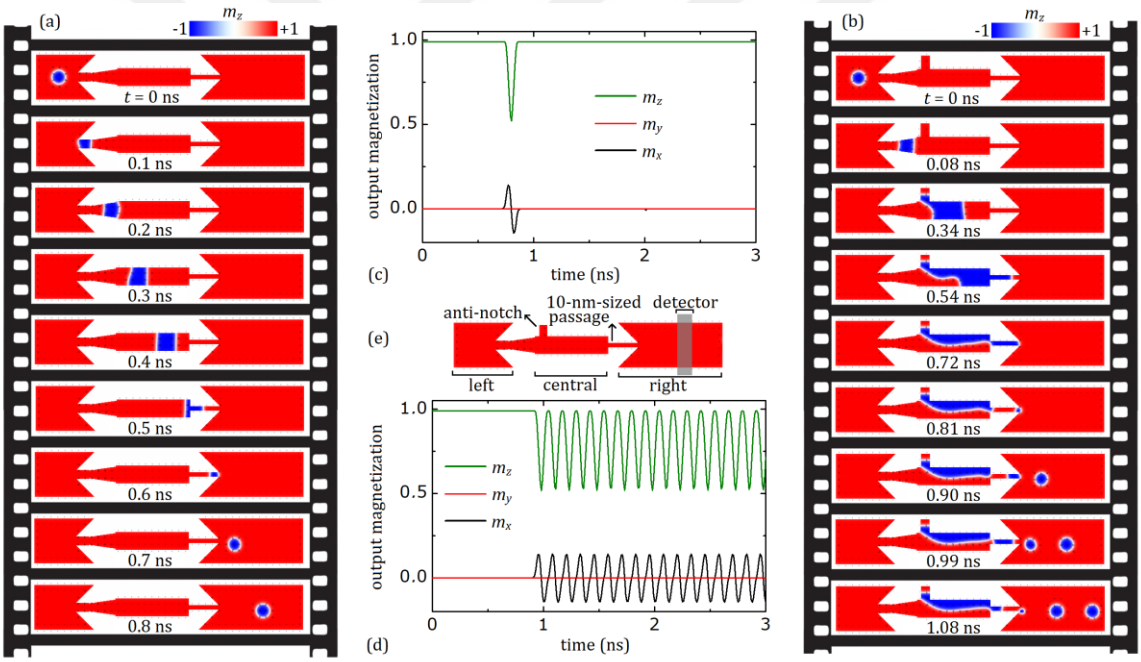

Figure 3.1 Reversible conversion between skyrmion-DW pair and coherent skyrmion generation. (a) A skyrmion created in the left chamber of the nanotrack. Then, it is drifted by current to the central chamber without the anti-notch, by transforming into a DW pair. Finally, it is, again, converted to the skyrmion by the passage in the entrance of right chamber. A current density of 7 TAm^{-2} is applied along -x for 3 ns. However, the spatial magnetization is represented as frames for 0 ns<t<0.8 ns to show the conversion process in more detail. (b) The coherent skyrmion generation after introducing the central chamber to the anti-notch with the dimensions of w=20 nm, l=30 nm. The current density is again 7 TAm^{-2}. Selected frames of the skyrmion generation process is represented from t=0 ns to

t=1.08 ns. (c) x,y and z components of the total magnetization in the detector area (output magnetization) with respect to simulation time in the absence of anti-notch. (d) The output magnetization with respect to simulation time in the presence of anti-notch. (e) Skyrmion generator with the detector. The detector has the width of 30 nm and length (height) of 100 nm and its center is located at 85 nm far from the end of the right chamber.

The story is a lot different when an anti-notch introduced to the central chamber, as can be seen in Figure 3.1(b). The current-driven skyrmion again moves to the rightward direction and is converted into a DW pair after t=0.08 ns elapsed. Once the DW pair reaches to the anti-notch, one side of the DW pair is pinning inside the anti-notch while the other side continues to flow toward the end of the central chamber, causing an expansion in the domain dimensions until t=0.54 ns. Addition of an anti-notch to the wire also results in an inhomogeneity in the current flow; i.e. an additional current component along the y axis. Inhomogeneous effective forces on the DWs caused by inhomogeneous current act to narrow the domain around the entrance of the 10-nm-sized passage, which is located at the end of the central chamber. This narrowing results in the breaking of the stripe at t=0.72 ns. The broken part (remained at the end of central chamber) of the DW propagates to the entrance of the 10-nm-sized passage until t=0.81 ns, at the same time, the clipping part of the stripe starts to “blow” a magnetic skyrmion bubble. Inhomogeneous effective forces, this time, act to expand the end of the domain in the entrance of the right chamber of the nanowire. As the domain end expands its radius, the surface tension in the DW (originated from the increasing in the energy of DW comprises the combination of exchange and anisotropy fields) increases [61, 63], resulting in the formation of the skyrmion until t=0.90 ns. This process resembles how liquid droplets are formed by leaking tap, which allow us to call these skyrmions as "skyrmion droplets". The periodic repetition of the process enables the coherent generation of the skyrmions.

We embedded a fictitious detector on the right chamber of the nanotrack, as can be seen in Figure 3.1(e), to reveal the time evolution of the skyrmion generation, especially the frequency. The detector measures the x,y and z components of the total normalized magnetization during simulations, lasting for 3 ns, and will be called as output magnetization. In Figure 3.1(c), the peaks of m_x and m_z corresponds to signal of skyrmion passage through the detector in the central chamber without an anti-notch (see Figure 3.1(a)) around t=0.8 ns. No skyrmion propagation is observed after t=0.8 ns, which indicates no multiple skyrmion generation in the absence of anti-notch. Figure 3.1(d) represents the output magnetization of anti-notch added geometry. It can be seen that multiple skyrmion generation in the right chamber is stable and coherent during the

simulation. To investigate the response of multiple skyrmion generation to alternating current, we calculate the time dependence of output magnetization by switching the applied current at random instants during the simulation. The results are represented in Figure 3.2. We found that the multiple skyrmion generation is sustainable with the switched current, which is obviously important for magnetic data storage applications. For the selected parameters, the generation frequency is 8.33 GHz. The frequency can be altered by both the intrinsic parameters of the material, i.e. the ratio of damping and non-adiabatic torque coefficients, and applied current.

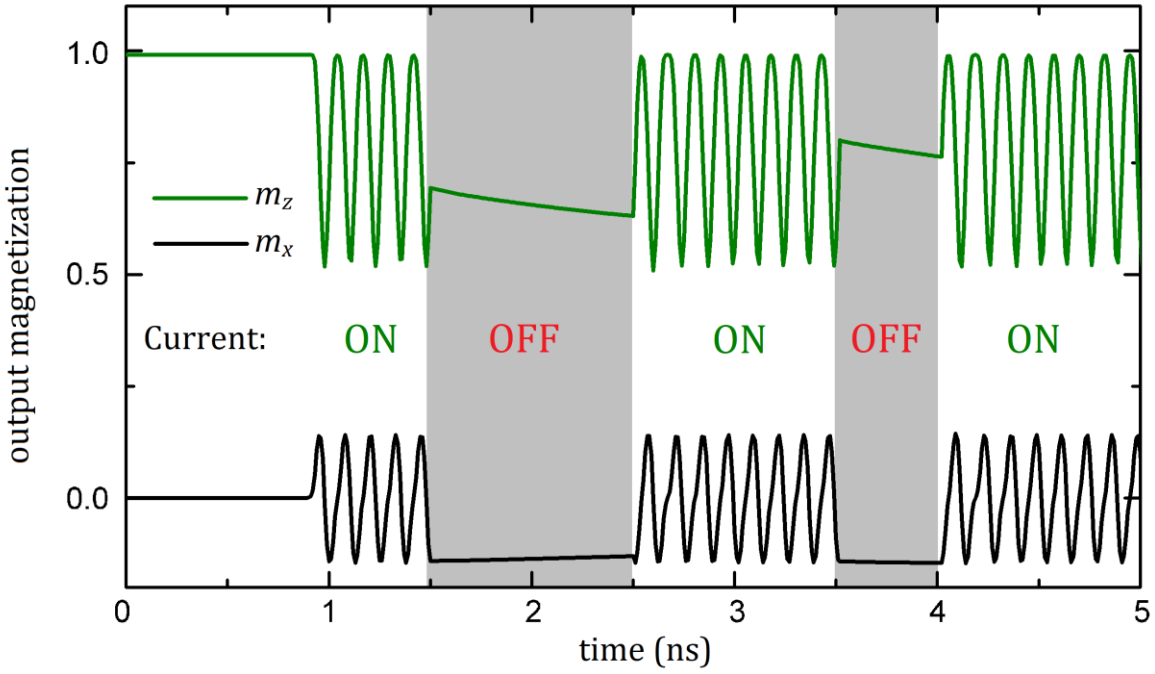

Figure 3.2 Sustainability of multiple skyrmion generation. The response of multiple skyrmion generation to switching of the current at random moments. The current density, *j*, of 7.0 TAm^{-2} is applied when the current is switched on. The anti-notch dimension of *w* = 20 nm and *l* = 30 nm is employed.

3.1.2. Current Density-Generation frequency relationship

Here, we study the impact of current density and α/β ratio on the dynamics of coherent skyrmion generation. We quantify the generation frequency, *f*, and drift velocity, $\vec{v}_s$, of the skyrmions. We scanned *f* and $\vec{v}_s$ as a function of current density *j* for three values of α/β. The results are shown in Figure 3.3(a) and Figure 3.3(b), respectively. For all values of α/β, we find a linear relationship between *j* and *f*, $\vec{v}_s$, that is, larger current density induces relatively high generation frequency and drift velocity. We find a threshold current density of 6.5 TAm^{-2}, i.e. the

minimum current density (j_m) required to blow a skyrmion from the 10-nm-sized passage. It can also be seen that, smaller values of α/β result in higher generation frequency and drift velocity since lower damping in the system allows faster motion of skyrmions. By applying j_m for α/β =1, we can generate skyrmions with drift velocity of 580 m/s corresponding to a reading speed of 6.4 Gb/s for a single race-track memory, given that the separation between each skyrmion is ~90 nm. The reading speed can be enhanced up to 18.4 Gb/s for a single track with a skyrmion separation distance of ~50 nm, by applying current density of 9.5 TAm^{-2}, for α/β =0.73. Using simultaneous multiple race-tracks can also increase the reading speed. The current-driven mobility of the skyrmions [64], μ=ν/*j*, was found to be roughly 92 ms^{-1}/TAm^{-2}, which is nearly independent of α/β.

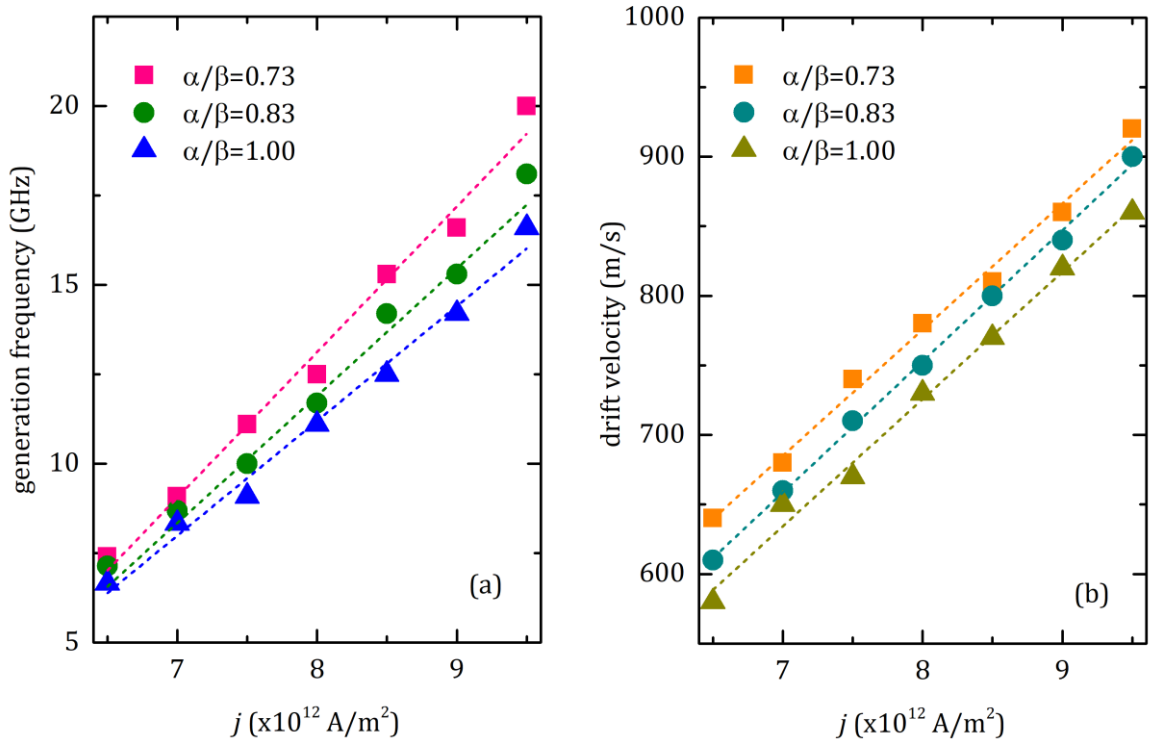

Figure 3.3 Skyrmion generation with respect to current. (a) The dependency of number of skyrmions generated per second on current density, *j*, for the anti-notch dimension of *w* = 20 nm and *l* = 30 nm. We changed *j* from 6.5 TAm^{-2} to 9.5 TAm^{-2} with the steps of 0.5 TAm^{-2} for various α/β ratios. β is remained at 0.3 while α is varied to get desired α/β ratio. (b) Drift velocity of skyrmions as a function of current density. Dashed lines in each figure are the linear fits of the corresponding data. The linear fits in (b) are used to extract the mobility (velocity per current density) of the skyrmions.

3.1.3. The role of anti-notch dimension

Even though we find that the embedding of the anti-notch results in the coherent skyrmion generation, there must be limitations for certain anti-notch width and length. Inserting the anti-notch to the central chamber gives rise to inhomogeneity in the current flow which corresponds to an additional current component along the y axis. The

magnitude of the y-component of the current is strongly correlated with the aspect ratio of the anti-notch. Moreover, the pinning of the backside of the DW pair depends on the magnitude of the y-component. To investigate the cases of which anti-notch dimensions disrupt multiple skyrmion generation, we performed simulations for anti-notches having two different dimensions, as shown in Figure 5. The width of the anti-notch remains constant while the length is determined as 25 nm and 45 nm in Figure 5(a) and Figure 5(b), respectively. In this case, the anti-notch in (a) and that of in (b) will be called as short and long anti-notch. The short anti-notch induces inadequate current flows toward the anti-notch, followed by passing of DW pair without pinning. Consequently, the coherent generation process does not occur, as can be seen in Figure 5(c). The anti-notch with redundant length can also prevent the generation. In Figure 5(b), the long anti-notch is embedded to the central chamber and current is applied. We noticed that long anti-notch induces large magnitude of y-component in current, which splits the DW pair around the anti-notch. In this case, residual part of the DW leaks in the anti-notch while the other part flows toward the right chamber and creates a single skyrmion. Even though the residual part in the anti-notch can create magnetic domains with the opposite direction of the magnetization of the nanowire, the domains can not reach the 10-nm-sized passage by vanishing at the upper-right edge of the central chamber. Figure 5(d) represents the time evolution of an unsuccessful coherent skyrmion generation by a long anti-notch.

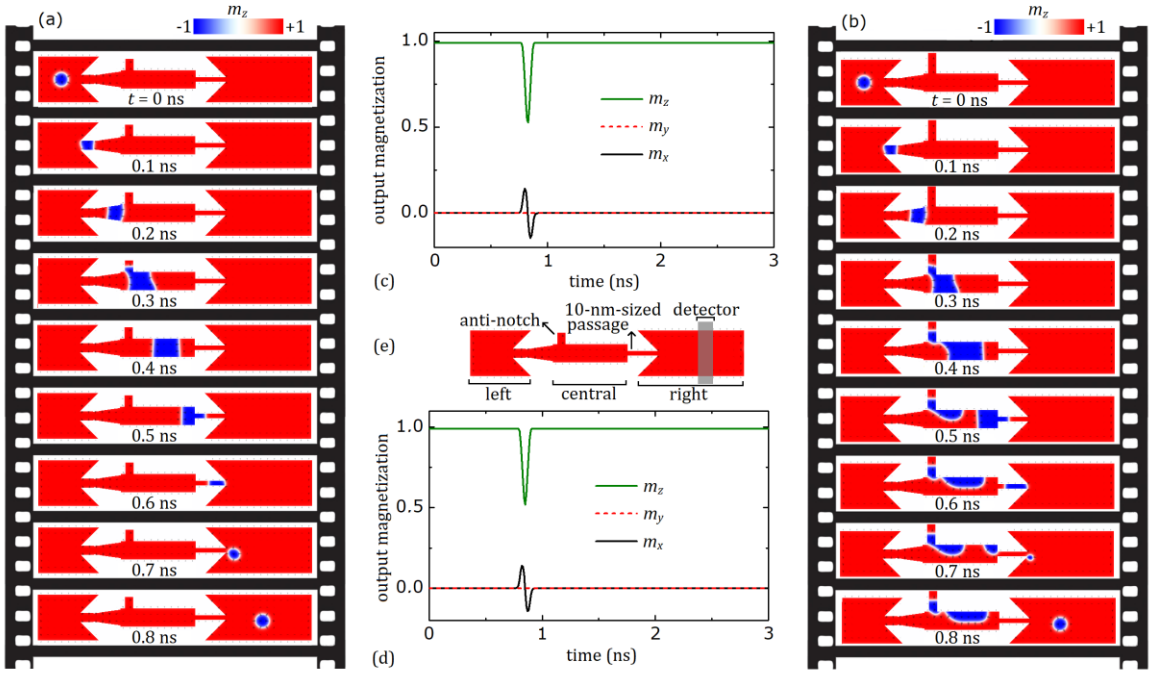

Figure 3.4 Two different anti-notch which prevent coherent skyrmion generation. The central chamber is introduced to an anti-notch with the dimensions of w=18 nm, l=25 nm

in (a) and w=18 nm, l=45 nm in (b). A current density of 7 TAm^{-2} is applied along –x for 3 ns. The spatial magnetization is represented as frames for 0 ns<t<0.8 ns to show the role of anti-notch dimensions on generation process in more detail. The output magnetizations with respect to simulation time in the presence of short and long anti-notch is represented in (c) and (d), respectively. (e) The nanotrack used for the simulations with the detector.

We compiled the role of width and length of the anti-notch by performing further analysis to represent the full picture, as shown in Figure 6. We investigated the control of coherent skyrmion generation as a function of both width (w) and length (l) of the anti-notch. Green boxes correspond to the w and l values enabling a coherent generation of skyrmions while red boxes represent the anti-notch geometry preventing the multiple skyrmion generation, *i.e.* the output is a single skyrmion. It seems that there is a lower limit for l in multiple skyrmion generation, which corresponds to the skyrmion diameter. For lengths smaller than the skyrmion diameter, the DW pair passes through the central chamber without pinning. For l=30 nm, we can observe all of the three scenarios: (1) the splitting of the DW pair followed by no coherent skyrmion generation for w=10 nm, (2) coherent skyrmion generation by the optimum aspect ratios for w=14-22 nm, (3) passing of the DW pair without pinning, again, followed by no coherent skyrmion generation for w>22 nm. For larger values of l=30 nm, the generation process becomes less “selective” since the only unfavorable scenario is the splitting of the DW pair by excessively long anti-notches.

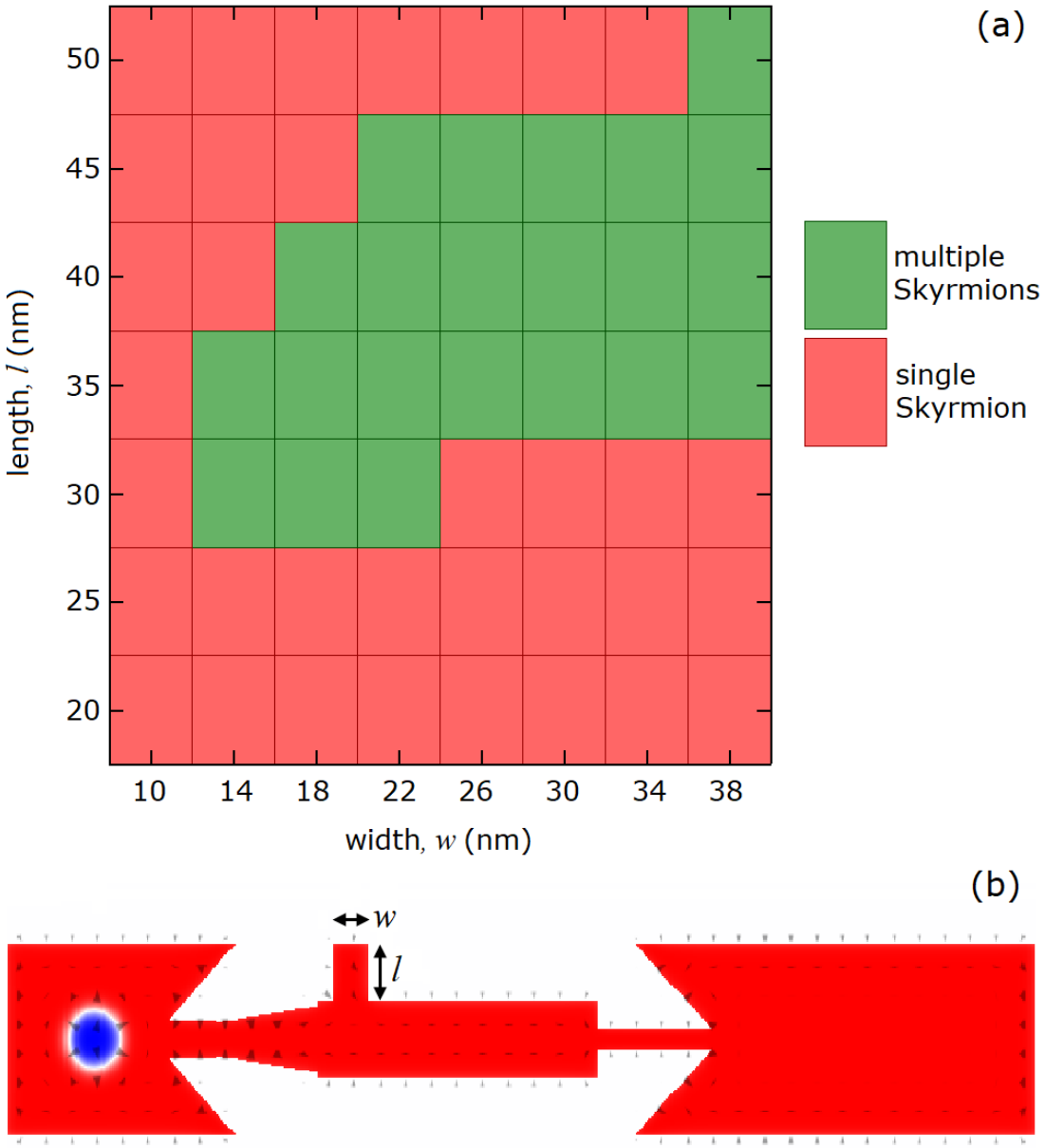

Figure 3.5 Dependency of coherent generation process on width and length of the anti-notch. (a) The effect of width w and length l on skyrmion generation. In the matrix, *w* and *l* values allowing coherent generation of skyrmions are represented by green boxes whereas the anti-notch geometries unfavorable for the generation appears as red. (b) The schematic representation of the nanotrack with anti-notch.

Additionally, the working conditions of successful coherent skyrmion generation for various material parameters are under investigation. Uniaxial magnetic anisotropy (K_1) and exchange stiffness (A_{ex}) affect the coherent skyrmion generation since they change the dimensions of reverse domains in the nanotrack. Thus, we prepared one more matrix chart to demonstrate the effect of the parameters on multiple skyrmion generation.

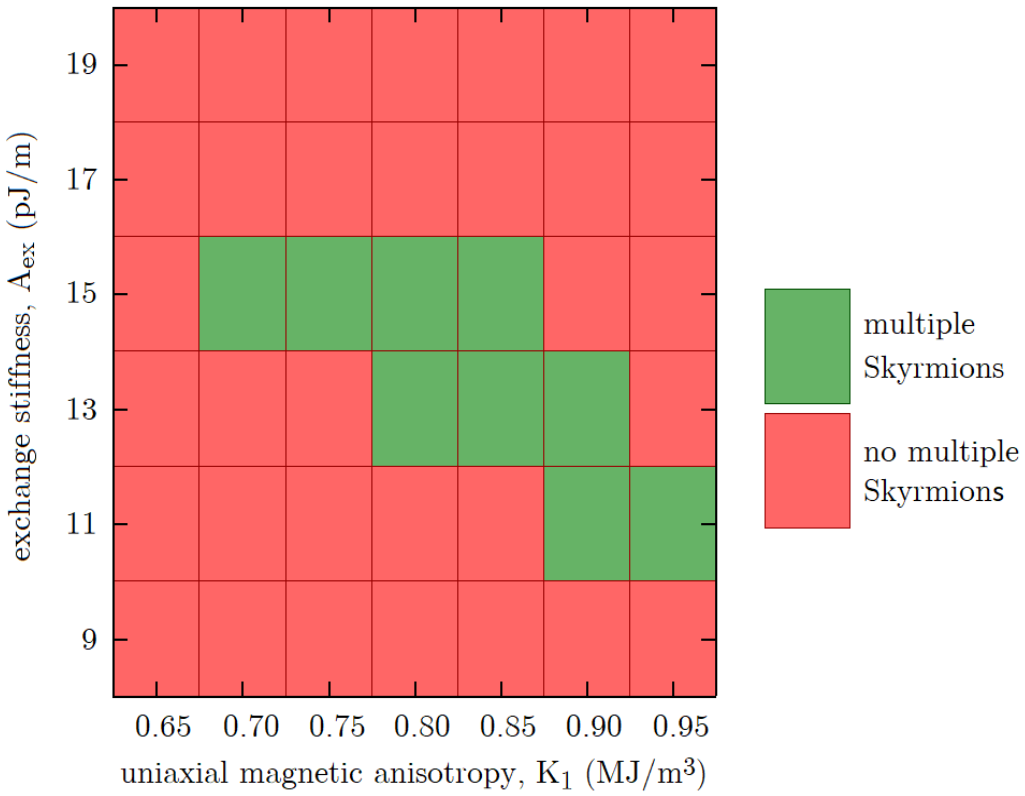

Figure 3.6 The matrix chart represents the dependency of multiple skyrmion generation on uniaxial magnetic anisotropy (K_1) and exchange stiffness (A_{ex}).

3.1.4. Usage of the Generation in a Racetrack Memory

We represent our further simulations that show writing-reading process does not slow down the coherent generation. First, we lengthened the right chamber to embed two additional components: a writing head, i.e. local magnetic field which can be produced by a nanowire, and a reading head, i.e. calculation of the z-component of total magnetization in a certain region. Thus, we are able to resemble a racetrack memory, which was first proposed in [7]. Then, we applied external magnetic field in a certain region which we named as the “writing head”, taking into account the period of skyrmion passing through the region. We applied 5 sequential field pulses of 0.8 T, which can be reduced by tailoring the material parameters and/or geometry, to erase the skyrmions. The effect of these deletings are detected approximately 0.3 ns later, since the traveling of 200 nm distance between writing and reading heads takes about 0.3 ns, as can be seen in Figure 3.7.

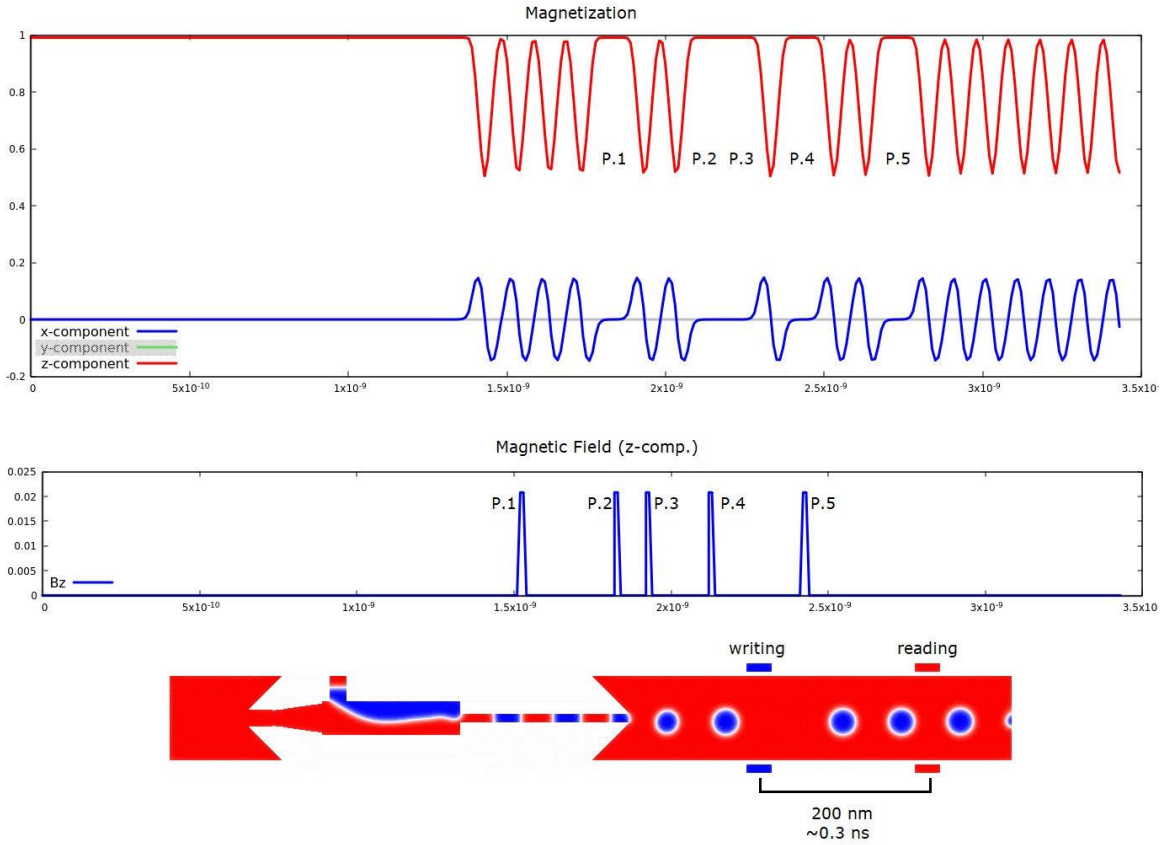

Figure 3.7 Writing-reading process in a racetrack by using the proposed skymion generator.

3.2. Impact of Interlayer Exchange Coupling on Magnetic Skyrmions

In addition to the generation, stability and motion; controlling the size of the skyrmions is also crucial for advanced skyrmionic applications. For this, most recent studies have focused on understanding both internal effects, such as strength of the magnetic anisotropy, and external effects such as magnetic field or electric current, on skyrmion size [65-67]. Controlling the skyrmion size without any external effect or any change in properties of each magnetic layer can be carried out via alternative approaches.

In this work, we propose a novel approach to control and manipulate the skyrmion size in coupled magnetic thin-film stacks consist of two ferromagnetic layers; a $[Pt/Co]_2$ layer and thicker single layer of Co seperated by a non-magnetic spacer, which allows a long-range Ruderman-Kittel-Kasuya-Yosida (RKKY) exchange coupling between the layers. Stabilization of the skyrmions by the RKKY interactions have been recently reported in the literature [68-70]. Here, to the best of our knowledge, we show, for the first time, that skyrmion diameter can be systematically controlled by the RKKY interactions as well as the external magnetic fields. We anticipate that our study not only offers further

insight into the rationalizing skyrmion size but also will inspire future discussions about the influence of the RKKY interaction on skyrmions.

3.2.1. Skyrmions in Coupled Layers

The procedure mentioned in Sec. II allowed us to observe helical and consequently skyrmion lattice phase. The domains of skyrmion lattice and spin spiral phases during the first-order phase transition are also observed for certain combinations of RKKY constant (J_{RKKY}) and magnetic field. In Figure 3.8(a), the white regions correspond to magnetization aligned to the direction of external magnetic field, while the magnetization of colored regions have in-plane components. Two simulation cells with zero z-component of magnetization on radial line are determined and the distance between them is attributed as skyrmion diameter. In the absence of RKKY coupling between Pt/Co and Co layers, skyrmion phase with skyrmion size of 17 nm are observed under 750 mT magnetic field. Then, we simulate the non-collinear system for different RKKY coupling constants to reveal the effect of the coupling on the skyrmion size. We perform the simulations for J_{RKKY} values from -0.2 to 0.2 mJ/m^2, as shown in Figure 3.8(b). Even if B_{ext} remains at 750 mT, skyrmion size is decreasing from 25.4 nm to 13.6 nm while J_{RKKY} is changing from -0.2 mJ/m^2 to 0.2 mJ/m^2. It can easily be seen that antiferromagnetic coupling results in larger skyrmions, whilst ferromagnetic coupling results in smaller skyrmions. This result is consistent with a recent analytical study by Bezvershenko et al.[68], which demonstrates the stabilizing effect of the RKKY interaction. The study investigates the effect in two different scenarios. One is the RKKY interaction through a normal metallic substrate, which is similar to our study in this thesis. The other is through single-layer graphene [68]. According to Bezvershenko et al., the effect of RKKY interaction in the energy of skyrmion has a negative impact which counteracts the skyrmion's tendency to vanish. It is also speculated that antiferromagnetic coupling leads strong contribution to survive the skyrmion, proportional to the diameter of magnetic skyrmion. However, unlike our procedure, the mangentic skyrmion stabilization scenario considered in [68] is based on the atomic framework and explicitly relies on crucial parameters, such as intralayer RKKY interaction and Fermi wavevector [68]. Even so, an in-depth investigation is needed to conclusively show the coordination of the micromagnetic and atomic frameworks.

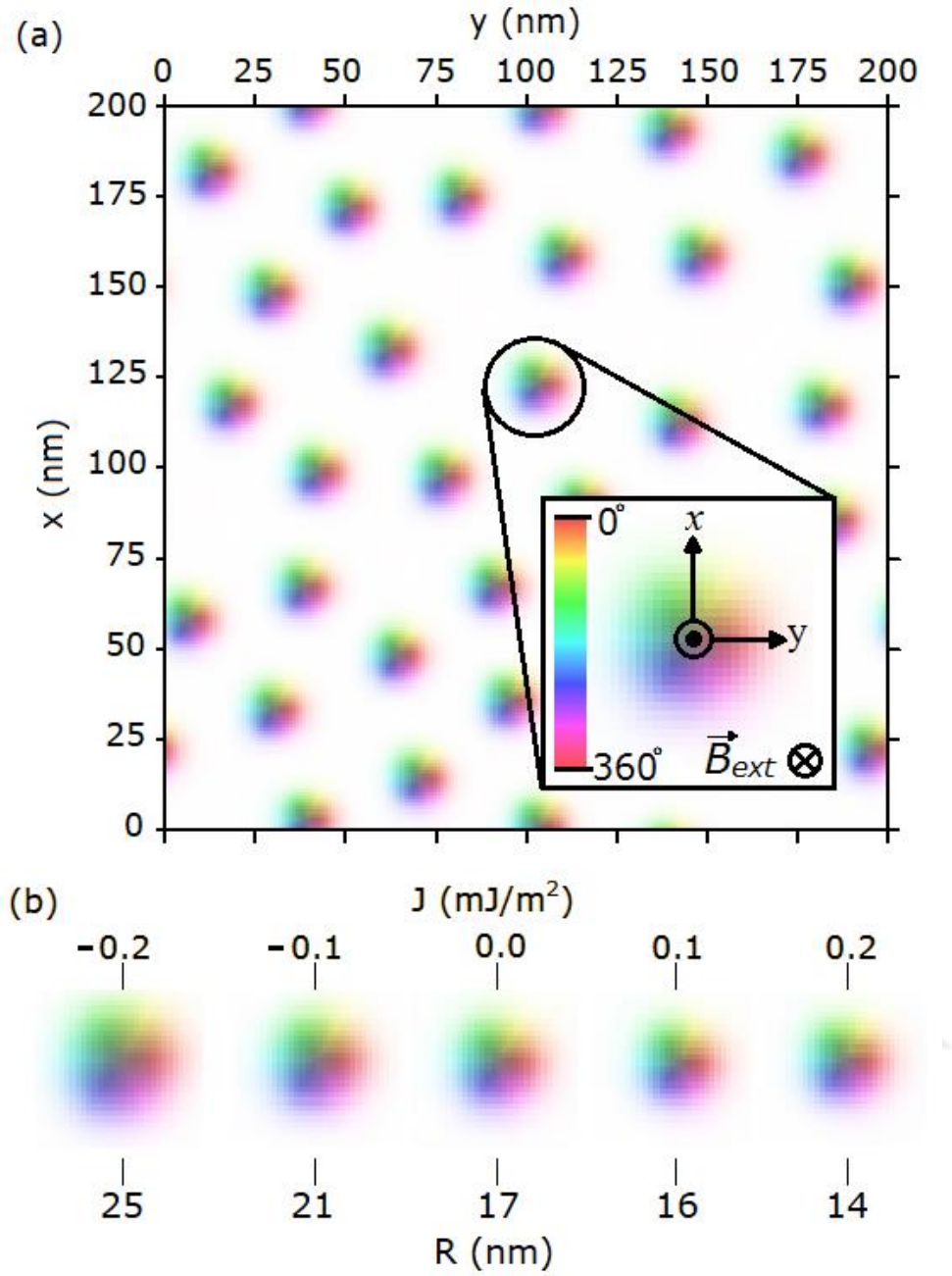

Figure 3.8 (a) Spatial magnetization of equilibrium skyrmion lattice phase for non-interacting case (J_{RKKY} =0.0 mJ/m^2) under external magnetic field of 750 mT. The initial state was almost ferromagnetic state with several metastable skyrmions as small as ~5 nm under external magnetic field of 1.5 T, then we gradually decrease the magnetic field to 750 mT. Simulated domain has the dimensions of 200 nm for both x and y directions. These parameters result in the skyrmion lattice phase with a diameter of 17 nm. The inset of (a) represents magnified spatial magnetization of a selected skyrmion with (*x*, *y*, *z*) coordinates used to describe the skyrmion structure. Polar orientation of cells represented by the color map. (b) Spatial magnetization of randomly selected skyrmions in the lattices belong to various RKKY constants from -0.2 mJ/m^2 to 0.2 mJ/m^2 (B_{ext}=750 mT).

We perform extensive calculations to understand the origin of larger skyrmions for antiferromagnetic coupling in micromagnetic framework. This time, as shown in Figure 3.9, we focus on the z-component of the magnetization of individual layers, in the thin-film stack, with respect to external magnetic field for different RKKY constants. The magnetization of Pt/Co layer is set to be perpendicular to the film plane during the simulations. On the other hand, the magnetic easy axis of Co lies parallel to the film plane. Depending on the RKKY interaction, while the strength of the external magnetic field is increasing, the magnetization direction of Co layer is more or less canted away from the film plane. In the presence of the magnetic field, ferromagnetic coupling of RKKY tends the magnetization of Co parallel to that of Pt/Co, resulting a greater number of spins aligned to the direction of magnetic field, which causes the formation of smaller size of skyrmions. However, antiferromagnetic coupling of RKKY forces the z-component of Co to lie in the opposite direction of the magnetic field. The interplay between the external magnetic field and the antiferromagnetic RKKY coupling results in a smaller number of spins aligned to the direction of the magnetic field, which allows the formation of larger skyrmions. In other words, the sum of the external magnetic field and ferromagnetic RKKY coupling dominates the system, which generates smaller skyrmions. Oppositely, the cancellation of the forces caused by the external magnetic field and the antiferromagnetic RKKY coupling allows Dzyaloshinskii-Moriya interaction to be dominant in the system which can lead to the generation of larger skyrmions. Also, during the simulations, magnetic state of the thick Co layer remains ferromagnetic while the state of Pt/Co layer is changing between spin spiral, skyrmionic and a mixed of them by changing external magnetic field and J_{RKKY}.

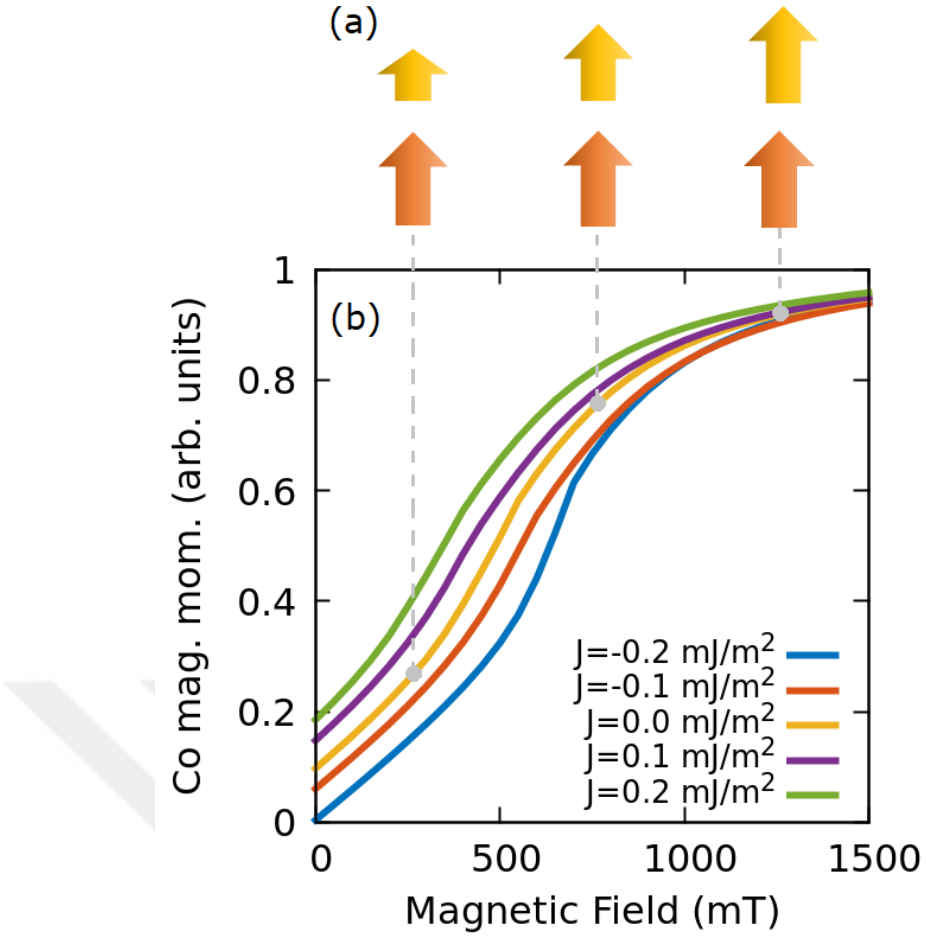

Figure 3.9 (a) Schematic representation of z-component of magnetization vectors under magnetic field of 250 mT, 750 mT and 1250 mT as indicated by gray vertical dashed lines. Here, yellow and orange vectors represent z-component of magnetization vector of Co and Pt/Co respectively. (J_{RKKY}=0) (b) Normalized magnetization of Co layer along z direction for various J values. The external magnetic field is also in the z direction and it is swept from 1500 mT to 0 mT.

3.2.2. Effect of Magnetic Anisotropy

We perform further calculations on the individual spatial magnetizations of layers, which is represented in Figure 3.10. We vary the uniaxial magnetic anisotropy constant of the top layer (without DMI) while magnetic anisotropy of bottom (Pt/Co) layer (with DMI) is constant under external magnetic field of 750 mT. For both of the AFM and FM couplings of the layers, skyrmions are formed in both of the layers but in the AFM case, having different directions as can be seen in Figure 3.10(a). We should emphasize that smaller values of uniaxial magnetic anisotropy allow the skyrmion formation in top layer, even if there is no intrinsic DMI in the layer, which lead us to call these skyrmions as "interlayer coupling induced skyrmions (ICIS)". For larger values of K_1, e.g. our 2.2 nm

thick Co, the layer has single domain behavior, and its magnetization direction changes with respect to the RKKY coupling.

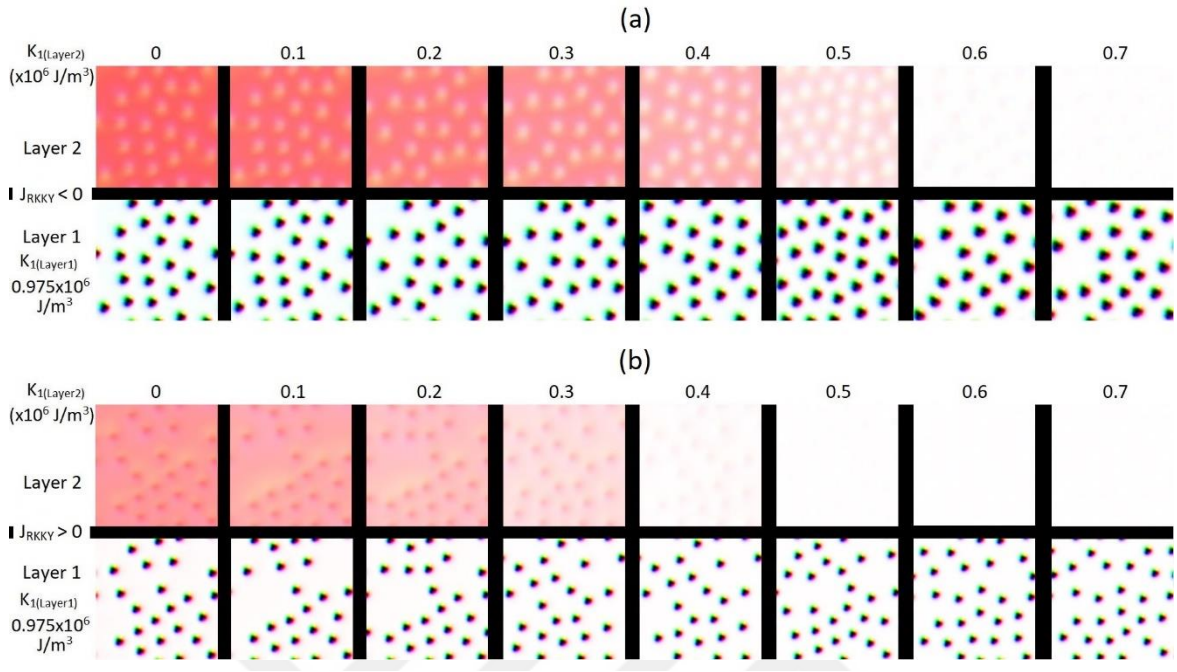

Figure 3.10 Spatial magnetizations of individual layers for different anisotropy constants of top layer in case of (a) antiferromagnetic coupling, J_{RKKY}=-0.2 mJ/m^2 and (b) ferromagnetic coupling, J_{RKKY}=0.2 mJ/m^2. The uniaxial magnetic anisotropy of Pt/Co layer is kept constant, $K_{1(Pt/Co)}$=0.975 x 10^6 J/m^3, while that of top layer is changing from 0 to 0.7 x 10^6 J/m^3. The external magnetic field is again 750 mT.

3.2.3. Zero Field Skyrmions

In the absence of the magnetic field, the skyrmion phase coexists with the helical phase independent of the coupling type, as seen in Figure 3.11(a)-(c). To reveal the relative stability of those phases, as shown in Figure 3.11(d)-(f), we perform energy density analyses on the phase domains, observed during the first-order phase transition. Here, we compare the energy densities of the skyrmion and helical domains for J_{RKKY}=-0.2 mJ/m^2. We find that the chosen skyrmion domain, shown in Figure 3.11 (d), is %4 higher in energy, corresponding to 16 kJ/m^3, as compared with that of the helical. On the other hand, the aforementioned assessments on the impact of the RKKY coupling on skyrmion size is still operative even in the case of zero magnetic field. However, the period of helical regions remains constant since we vary the RKKY constant by scaling the

exchange interaction only between two simulation layers. Then, the A_{ex}/D_i ratio determined for the layers remains unchanged which results in a constant period of helicals. Additionally, the remanent magnetization of the Co layer is decreased for the antiferromagnetic RKKY coupling. Besides, experimental observation of zero field skyrmions in Co/non-magnetic metal multilayers have been reported by recent studies [24, 32]. Zero field skyrmion lattice with helical phase was observed in Pt/Co/Ta multilayers by Zhang et al.[32]. Also, direct imaging of skyrmions in an exchange-coupled Co/Pd multilayer without a stabilizing out-of-plane field could be achieved recently by Pollard et al.[24]. Note that, the skyrmions imaged in both studies are Néel type skyrmions. Consequently, our results for the presence and absence of the magnetic field are in very good agreement with the recent experimental studies in this perspective.

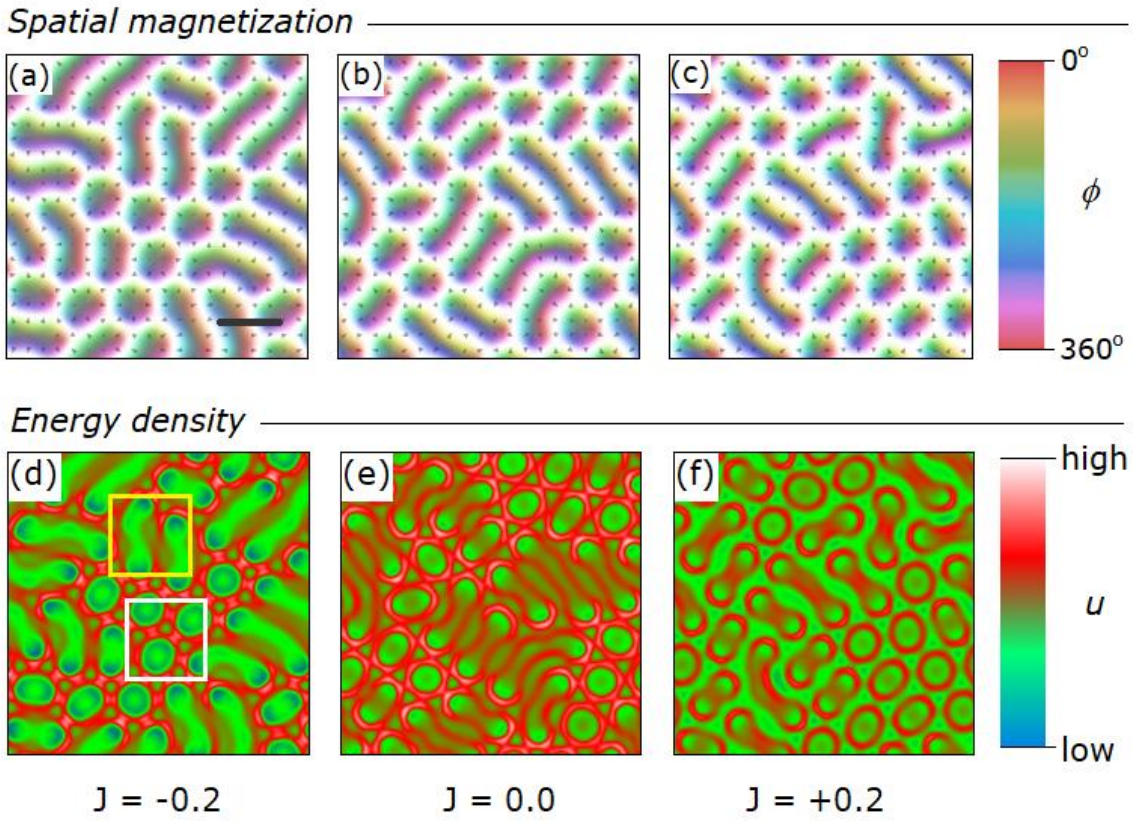

Figure 3.11 The spatial magnetization of the system without an external magnetic field (B_{ext}=0) for (a) J_{RKKY}=-0.2, (b) 0.0 and (c) 0.2 mJ/m^2. Different colors correspond to different polar orientations, ϕ, of the cells. Notably, the skyrmion domains at the zero field are observed for all types of coupling. Horizontal scale bar; 40 nm. The spatial energy density, u, maps for (d) J_{RKKY}=-0.2, (e) 0.0 and (f) 0.2 mJ/m^2. The white and yellow areas in (d) enclosing the skyrmionic and helical domains, respectively, are taken for relative energy evaluation (see text).

In order to get a better understanding of the evolution of the skyrmion size with respect to the RKKY coupling under magnetic field, we perform comprehensive simulations includes the systematic variation of both the external magnetic field and the RKKY coupling constant. To summarize our results and display the bigger picture, we show a heat map of skyrmion diameter. The results are shown in Figure 3.12. We also show two graphs to demonstrate the numerical interpretation of the heat map. The variations of the skyrmion diameter by the magnetic field for the slices of RKKY coupling and by the RKKY coupling for the slices of magnetic field are shown in Figure 3.12(a) and Figure 3.12(b), respectively. The skyrmion size is strongly dependent on the magnetic field for both coupling types, as can be seen in Figure 3.12(a). The magnetic field also affects the magnetic phase of the system which is not considered in detail here, since it requires a separate comprehensive effort which is beyond the scope of this study. But briefly; the coexistence of helical and skyrmion phase under low magnetic fields gives place to a sole skyrmion phase for stronger magnetic fields, based on our simulations. In Figure 3.12(b), the fluctuations of skyrmion diameter between J_{RKKY}= -0.1 mJ/m^2 and J_{RKKY}=0.0 mJ/m^2 are originated from the competition between relatively strong magnetic field of 750 mT and weak antiferromagnetic coupling of $|J_{RKKY}|<0.1$ mJ/m^2. In the case of weak ferromagnetic coupling of $0.0<|J_{RKKY}|<0.1$ mJ/m^2, strong magnetic field dominates the system resulting in an almost constant skyrmion diameter for the same magnetic field, even if the coupling constant is changed from 0.0 mJ/m^2 to 0.1 mJ/m^2. In Figure 3.12(c), the effects of magnetic field and RKKY coupling on the skyrmion diameter are clearly observed. The magnetic field reduces the skyrmion diameter for all J_{RKKY} values, as expected. Besides, the RKKY coupling strongly affects the size of the skyrmions with respect to the magnetization of Co layer in the direction of z-component.

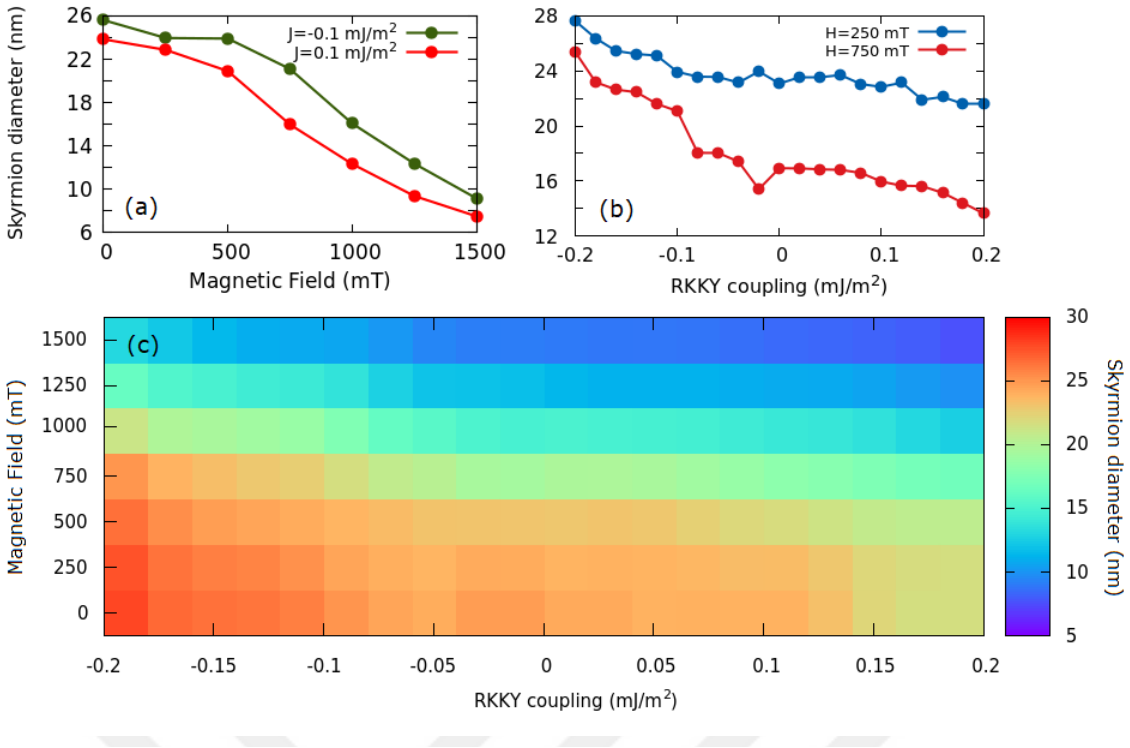

Figure 3.12 (a) The skyrmion diameter with respect to the magnetic field is shown for the RKKY coupling of J_{RKKY}=-0.1 and 0.1 mJ/m^2 with green and red lines, respectively. The trend of the decreasing diameter of antiferromagnetic and ferromagnetic coupling is similar. (b) The skyrmion diameter as a function of RKKY coupling under magnetic field of 250 mT and 750 mT. (c) The heat map of the skyrmion diameter versus RKKY coupling and magnetic field in the x and y directions, respectively.

3.3. Experimental Results

3.3.1. Hysteresis Curves

In order to observe spin spiral and skyrmion states, tailoring of magnetic properties of thin film structure is inevitable. We employ Pt/Co/Cu sandwich structure to induce perpendicular magnetic anisotropy and DMI interaction. However, the magnitude of the perpendicular magnetic anisotropy should not be large, avoiding force the system to a single domain state without spin spirals in the absence of magnetic field. For all samples used in this thesis, we fix the thickness of buffer layer of Pt as 4 nm and the thickness of the Co layer as 0.6 nm. The thin film structure with the thicknesses of the layers is represented in Figure 3.13, below.

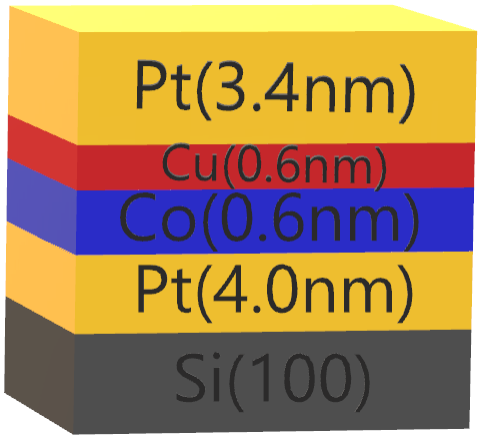

Figure 3.13 Si(100)/Pt(4nm)/Co(0.6nm)/Cu(0.6nm)/Pt(3.4nm)

For the structure, we were able to induce perpendicular magnetic anisotropy, as can be seen in the hysteresis curve (Figure 3.14). However, the remanence magnetization of the sample is almost equal to saturation magnetization, which indicates the absence of any helical phase. Here, the system is single-domain and the interface-induced DMI is not sufficient to modify domain structure of the sample.

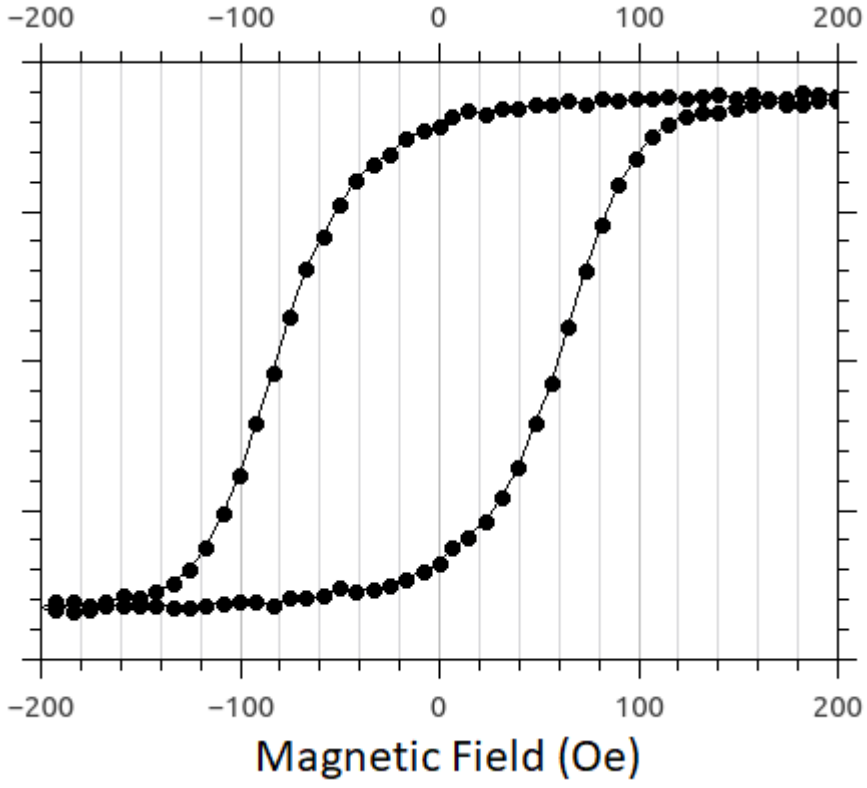

Figure 3.14 The hysteresis curve of Si(100)/Pt(4nm)/Co(0.6nm)/Cu(0.6nm)/Pt(3.4nm) measured in polar geometry

In order to reduce remanent magnetization of the sample while preserving perpendicular magnetic anisotropy, we increase the thickness of Cu layer from 0.6 nm to 1.2 nm. Here, we fix the total thickness of upper Pt/Cu layer as 4 nm by decreasing the thickness of Pt layer from 3.4 nm to 2.8 nm. The multilayer structure can be seen in Figure 3.15.

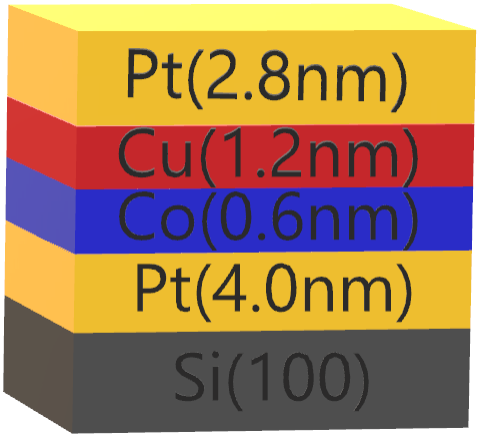

Figure 3.15 Si(100)/Pt(4nm)/Co(0.6nm)/Cu(1.2nm)/Pt(2.8nm)

This time, we were successful to reduce remanent magnetization and coercive field even if we can not vanish them completely. The hysteresis curve of the sample measured in polar geometry can be seen in Figure 3.16.

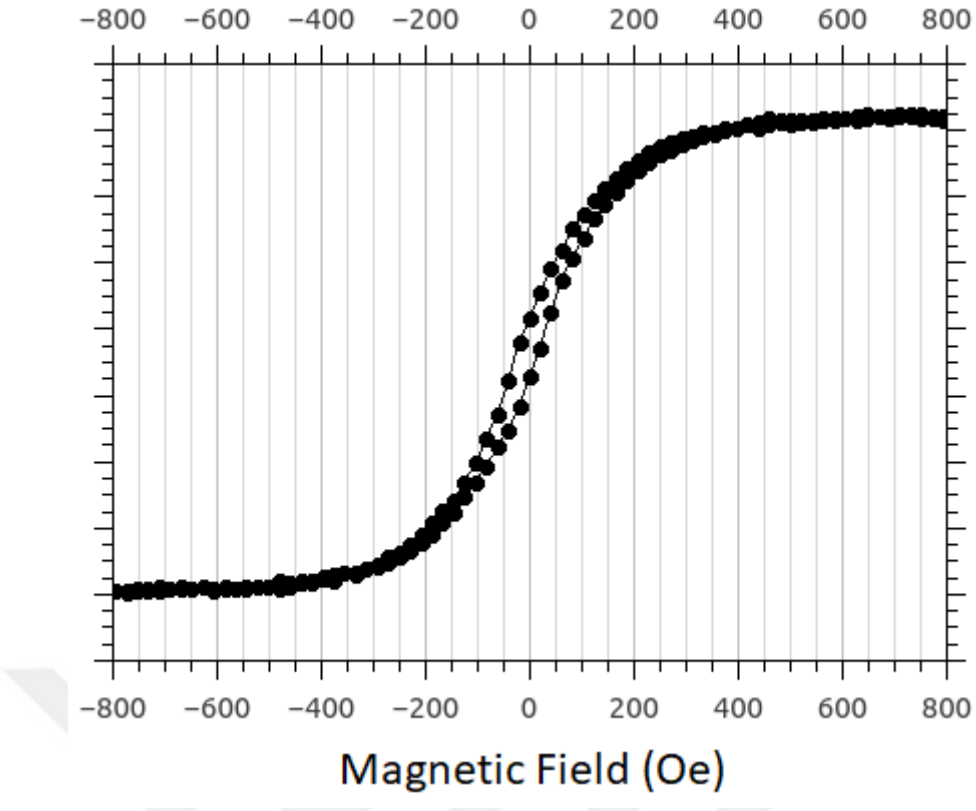

Figure 3.16 The hysteresis curve of Si(100)/Pt(4nm)/Co(0.6nm)/Cu(1.2nm)/Pt(2.8nm) measured in polar geometry

We, again, increase the thickness of Cu layer to 1.8 nm, which is maximum value for this thesis. The hysteresis curve of the sample is given in Figure 3.18.

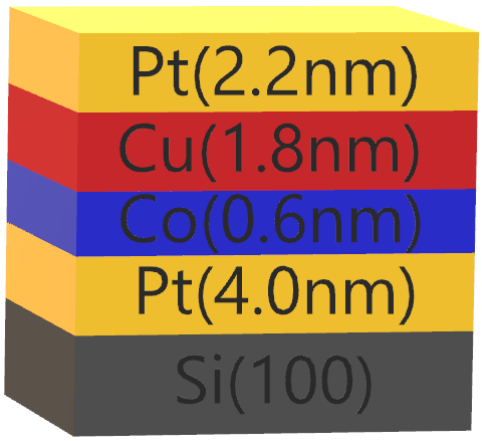

Figure 3.17 Si(100)/Pt(4nm)/Co(0.6nm)/Cu(1.8nm)/Pt(2.2nm)

Finally, the coercive field and remanent magnetization is almost vanished in Figure 3.18.

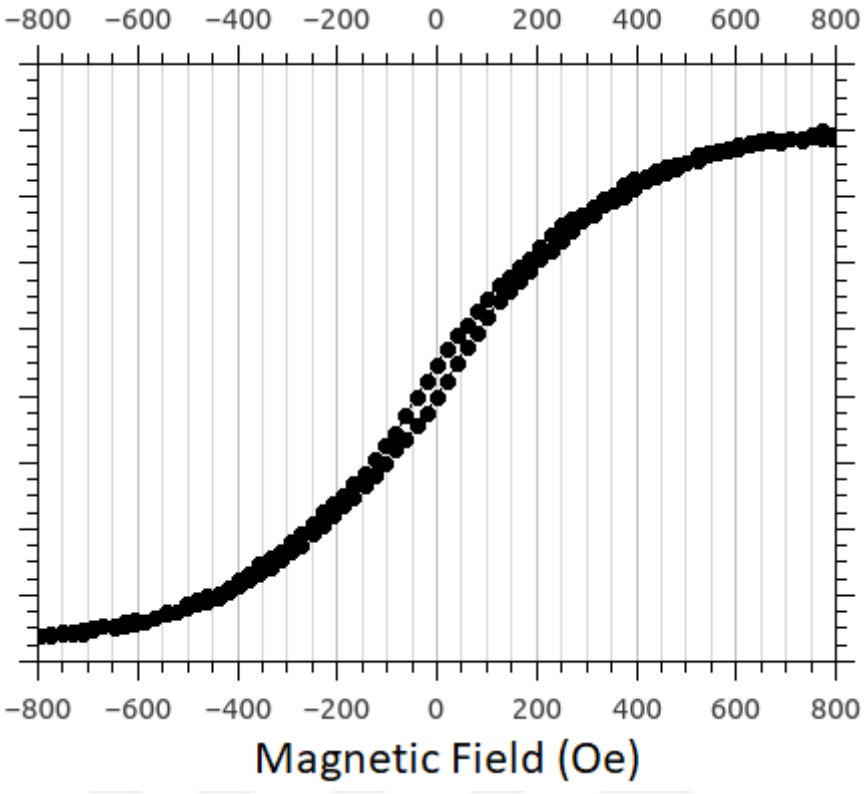

Figure 3.18 The hysteresis curve of Si(100)/Pt(4nm)/Co(0.6nm)/Cu(1.2nm)/Pt(2.8nm) measured in polar geometry

We obtain the desired hysteresis curve for polar geometry, however, we need to perform another measurement for longitudinal geometry, to be sure that our easy axis still laying to out-of-plane. The hysteresis curve measured in longitudinal can be seen in Figure 3.19.

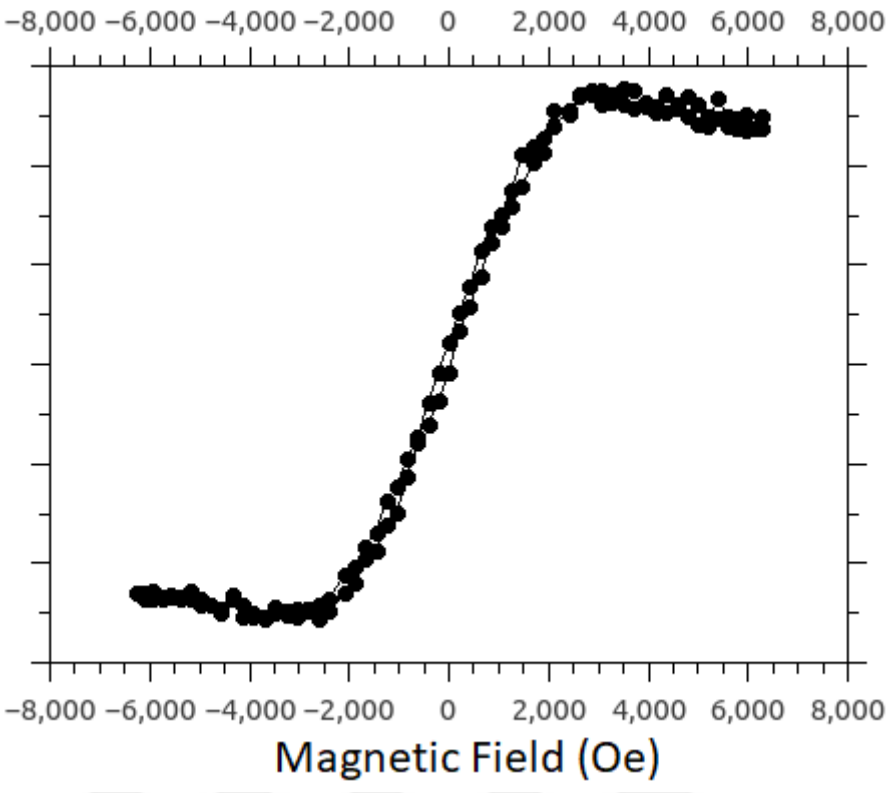

Figure 3.19 The hysteresis curve of Si(100)/Pt(4nm)/Co(0.6nm)/Cu(1.2nm)/Pt(2.8nm) measured in longitudinal geometry

Following the confirmation of the magnetically easy direction of the structure by comparing polar and longitudinal magneto-optic kerr effect measurements, we tried to increase the strength of magnetic signal in the surface of the thin film structure. The aim was enhancing the signal to be measurable for magnetic force microscopy with the similar hysteresis behavior obtained in Figure 3.18.

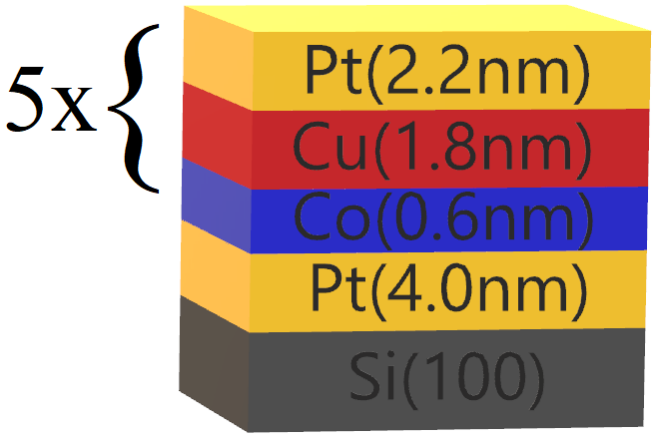

Figure 3.20 Si(100)/Pt(4nm)/[Co(0.6nm)/Cu(1.8nm)/Pt(2.2nm)]$_5$

Thus, we repeated Co(0.6nm)/Cu(1.2nm)/Pt(2.8nm) layers five times, as represented in Figure 3.20. The hysteresis curves for polar and longitudinal geometries can be seen in Figure 3.21 and 3.22, respectively.

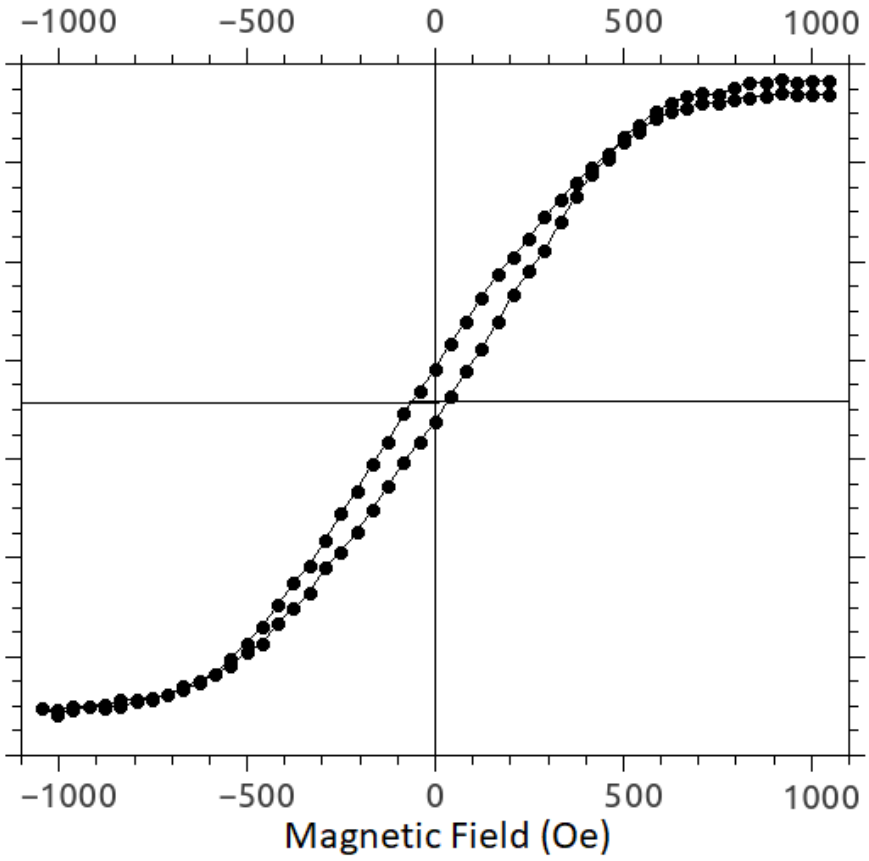

Figure 3.21 The hysteresis curve of Si(100)/Pt(4nm)/[Co(0.6nm)/Cu(1.2nm)/Pt(2.8nm)]$_5$ measured in polar geometry

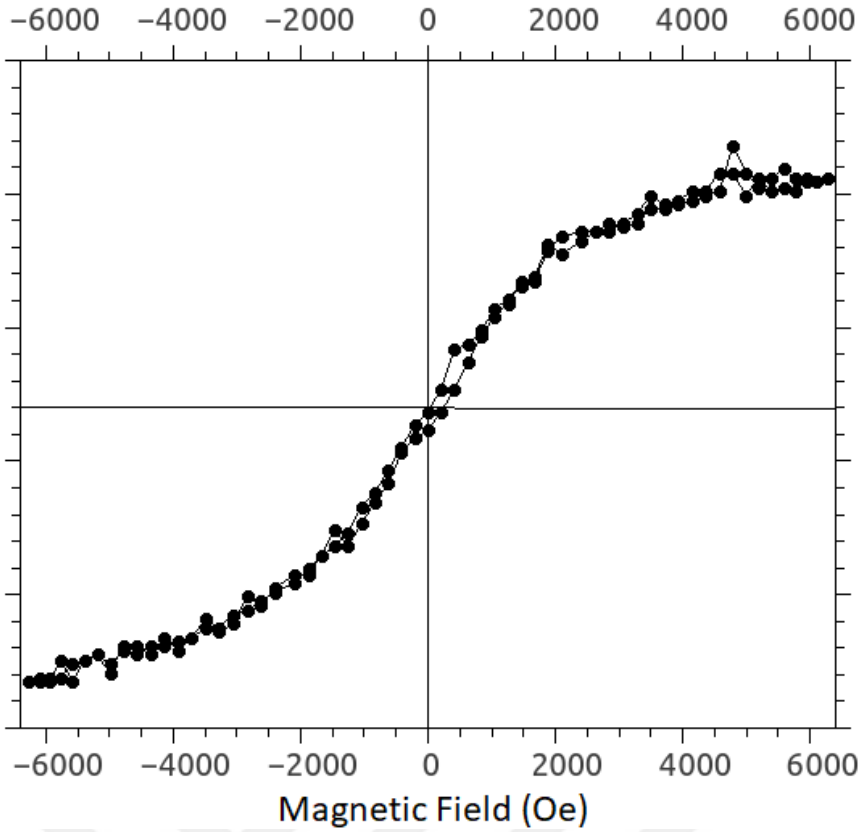

Figure 3.22 The hysteresis curve of Si(100)/Pt(4nm)/[Co(0.6nm)/Cu(1.2nm)/Pt(2.8nm)]$_5$ measured in longitudinal geometry

Finally, we were ready to observe spin spirals by magnetic force microscopy with this sample.

3.3.2. Magnetic Topography

We scanned the surface of Si(100)/Pt(4nm)/[Co(0.6nm)/Cu(1.2nm)/Pt(2.8nm)]$_5$ by magnetic force microscopy. The total measurement area was 10 µm x 10 µm. The tip was lifted 100 nm after the first scan. The spin spirals were successfully observed in the absence of external magnetic field in Figure 3.23.

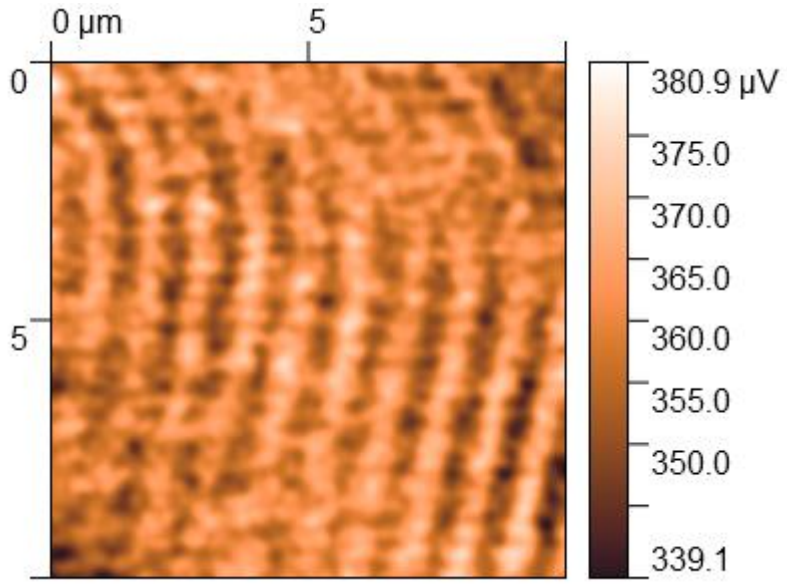

Figure 3.23 MFM image of Si(100)/Pt(4nm)/[Co(0.6nm)/Cu(1.2nm)/Pt(2.8nm)]$_5$

We also extracted line profile of the spin spirals in Figure 3.24. According to the measurements, the period of spin spirals was about 1 µm. The MFM system and magnetic tips does not allow performing a high resolution scan to spin spirals. Also we were not able to perform measurements under external magnetic field. After a set of modifications on the MFM system, we could apply magnetic field to the sample during the measurement, which can allow the observation of magnetic skyrmions.

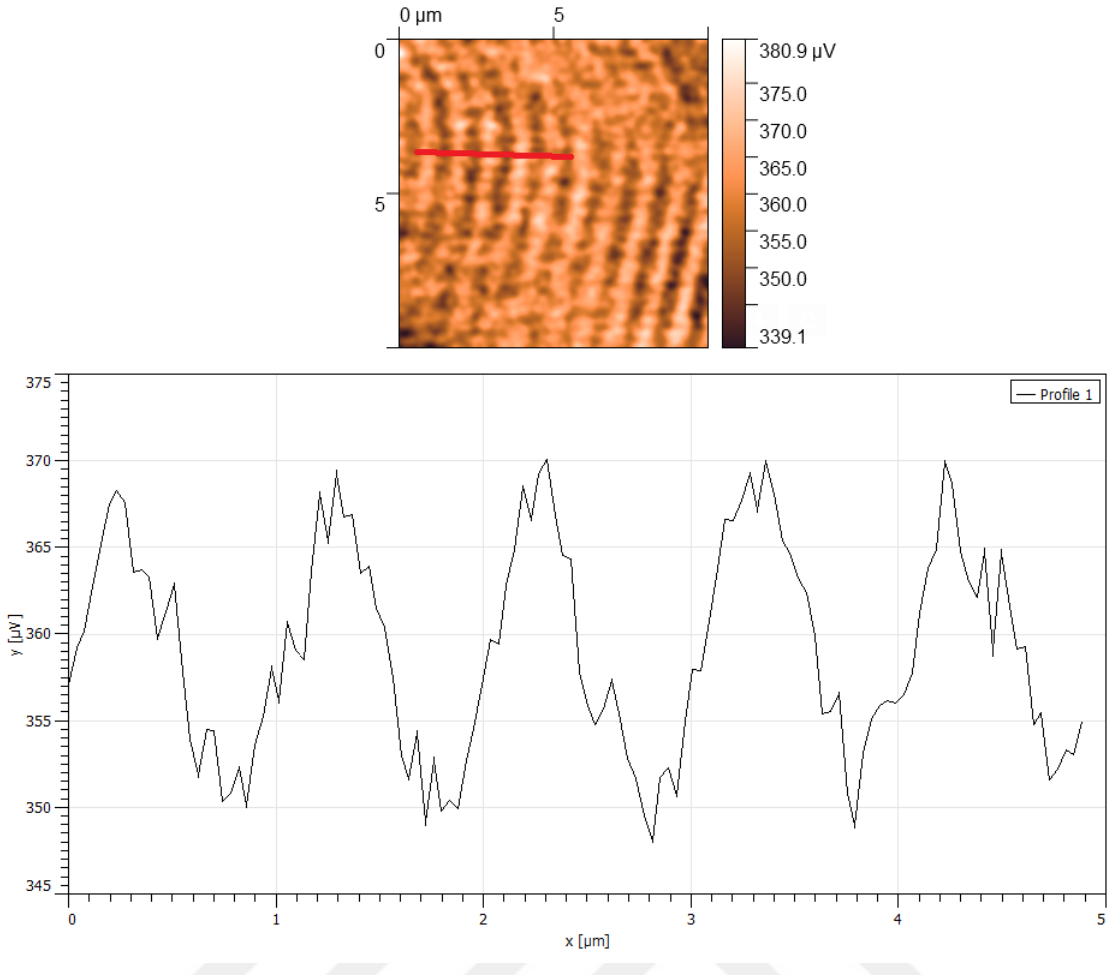

Figure 3.24 Line profile of the magnetic topography of the thin film multilayer structure Si(100)/Pt(4nm)/[Co(0.6nm)/Cu(1.2nm)/Pt(2.8nm)]$_5$. Here, x axis represent the red line in the MFM image.

4. CHAPTER 4 - CONCLUSIONS

In the first part of this study, we demonstrated a new road map for permanent current-driven coherent generation of magnetic skyrmions in the GHz frequency range, by embedding an engineered anti-notch to a nanotrack. We found that the anti-notch results in an inhomogeneity in the current flow which leads an electrical skyrmion oscillator producing a periodic chain of magnetic skyrmions without any periodic external influence. This procedure can be realized as an alternative method to the field and/or spin-polarized current pulsation in multiple skyrmion generation. The dynamics of current-driven skyrmion and DWs are extensively investigated as a function of the geometry of anti-notch and current density by micromagnetic simulations. The frequency of the generation and drift velocity of the skyrmions are also tailored by the applied current density. Moreover, skyrmion generation is crucially affected by both damping and nonadiabaticity parameters, as well as the geometry of the anti-notch. We found that the reading speed based on the generation can be enhanced up to 18.4 Gb/s for a single race-track, which can be increased by using multiple tracks.

In the second part of this study, we have considered the effect of the RKKY interaction on the skyrmion size for two magnetic layers separated by a non-magnetic spacer, where easy axes of magnetic layers are perpendicular to each other in non-interacting case. Through micromagnetic simulations, we observed that the formation of large or small sized skyrmions is strongly dependent on the type of the RKKY coupling, being either antiferromagnetic or ferromagnetic, respectively. We found that z-component of the magnetization of layers determines the skyrmion size, which can be controlled by the RKKY coupling. Interlayer coupling induced skyrmions are also formed in top layer (without DMI) for which has a weak uniaxial magnetic anisotropy. The size of the skyrmions at zero magnetic field can also be controlled by the interaction. Moreover, a mixed state of skyrmion lattice and helical phase is observed under zero magnetic field. We expect that our results will influence the development of advanced skyrmionic applications and should deserve further experimental studies to be comprehensively understood.

In the third part of the thesis, we experimentally growth thin film multilayer structure which allowed us to observe spin spiral state by MFM measurements. The strength of DMI interaction and perpendicular magnetic anisotropy was tailored by changing the thickness of Cu layer. Hysteresis curves of samples provided information about the magnetic state of the samples, especially in the absence of magnetic field, at first sight. The sample which has a structure of Si(100)/Pt(4nm)/Co(0.6nm)/Cu(1.2nm)/Pt(2.8nm), was chosen as a best candidate to observe spin spirals. In the case of the low signal intensity from the ultra-thin film multilayer structure for MFM measurements, we repeated Co(0.6nm)/Cu(1.2nm)/Pt(2.8nm) multilayers five times to increase the total amount of magnetic material existed in the structure, while preserving perpendicular magnetic anisotropy. The engineered structure, Si(100)/Pt(4nm)/$[Co(0.6nm)/Cu(1.2nm)/Pt(2.8nm)]_5$ was investigated by magnetic force microscopy and spin spiral state formed in the structure was revealed. The period of the spirals was also determined by using line profile of the magnetic topography of the thin film multilayer structure.

References

1. Silberman, N.A., et al., *The Oxford companion to archaeology*. 2012: Oxford University Press.
2. ; Available from: https://www.iflscience.com/technology/how-much-data-does-the-world-generate-every-minute/.
3. Gantz, J. and D. Reinsel, *The digital universe in 2020: Big data, bigger digital shadows, and biggest growth in the far east.* IDC iView: IDC Analyze the future, 2012. **2007**(2012): p. 1-16.
4. Clark, M.H., *Making magnetic recording commercial: 1920–1955.* Journal of magnetism and magnetic materials, 1999. **193**(1-3): p. 8-10.
5. Piramanayagam, S. and T.C. Chong, *Developments in data storage: materials perspective*. 2011: John Wiley & Sons.
6. 23.04.2019]; Available from: http://www.microscopyuk.org.uk/mag/indexmag.html?http://www.microscopyuk.org.uk/mag/art98/hdrive.html.
7. Parkin, S.S., M. Hayashi, and L. Thomas, *Magnetic domain-wall racetrack memory.* Science, 2008. **320**(5873): p. 190-194.
8. Cullity, B.D. and C.D. Graham, *Introduction to magnetic materials*. 2011: John Wiley & Sons.
9. Dzyaloshinskii, I.E., *On the magneto-electrical effects in antiferromagnets.* Soviet Physics JETP, 1960. **10**: p. 628-629.
10. Moriya, T., *Anisotropic superexchange interaction and weak ferromagnetism.* Physical Review, 1960. **120**(1): p. 91.
11. van Dijk, B., *Skyrmions and the dzyaloshinskii-moriya interaction*. 2015.
12. Kasuya, T., *A theory of metallic ferro-and antiferromagnetism on Zener's model.* Progress of theoretical physics, 1956. **16**(1): p. 45-57.
13. Ruderman, M.A. and C. Kittel, *Indirect exchange coupling of nuclear magnetic moments by conduction electrons.* Physical Review, 1954. **96**(1): p. 99.
14. Yosida, K., *Magnetic properties of Cu-Mn alloys.* Physical Review, 1957. **106**(5): p. 893.
15. Stiles, M.D., *Interlayer exchange coupling.* Journal of Magnetism and Magnetic Materials, 1999. **200**(1-3): p. 322-337.
16. Bruno, P. and C. Chappert, *Erratum: Oscillatory coupling between ferromagnetic layers separated by a nonmagnetic metal spacer [Phys. Rev. Lett. 67, 1602 (1991)]*. Physical Review Letters, 1991. **67**: p. 2592.
17. Bruno, P. and C. Chappert, *Interlayer Exchange Coupling: RKKY Theory and Beyond*, in *Magnetism and Structure in Systems of Reduced Dimension*. 1993, Springer. p. 389-399.
18. Yildiz, F., M. Przybylski, and J. Kirschner, *Perpendicular anisotropy and oscillatory interlayer coupling in Fe 0.5 Co 0.5/Rh/Fe 0.5 Co 0.5 bilayers on Rh (001).* Journal of Applied Physics, 2009. **105**(7): p. 07C312.
19. Yildiz, F., M. Przybylski, and J. Kirschner, *Direct Evidence of a Nonorthogonal Magnetization Configuration in Single Crystalline Fe 1− x Co x/Rh/Fe/Rh (001) System.* Physical review letters, 2009. **103**(14): p. 147203.
20. Fert, A., V. Cros, and J. Sampaio, *Skyrmions on the track.* Nature nanotechnology, 2013. **8**(3): p. 152.
21. Yu, X., et al., *Near room-temperature formation of a skyrmion crystal in thin-films of*

the helimagnet FeGe. Nature materials, 2011. **10**(2): p. 106.
22. Luo, S., et al., *Reconfigurable skyrmion logic gates.* Nano letters, 2018. **18**(2): p. 1180-1184.
23. Münzer, W., et al., *Skyrmion lattice in the doped semiconductor Fe 1− x Co x Si.* Physical Review B, 2010. **81**(4): p. 041203.
24. Pollard, S.D., et al., *Observation of stable Néel skyrmions in cobalt/palladium multilayers with Lorentz transmission electron microscopy.* Nature communications, 2017. **8**: p. 14761.
25. Sampaio, J., et al., *Nucleation, stability and current-induced motion of isolated magnetic skyrmions in nanostructures.* Nature nanotechnology, 2013. **8**(11): p. 839.
26. Xing, X., P.W. Pong, and Y. Zhou, *Skyrmion domain wall collision and domain wall-gated skyrmion logic.* Physical Review B, 2016. **94**(5): p. 054408.
27. Yu, X., et al., *Real-space observation of a two-dimensional skyrmion crystal.* Nature, 2010. **465**(7300): p. 901.
28. Zhang, X., M. Ezawa, and Y. Zhou, *Magnetic skyrmion logic gates: conversion, duplication and merging of skyrmions.* Scientific reports, 2015. **5**: p. 9400.
29. Zhang, X., et al., *Magnetic skyrmion transistor: skyrmion motion in a voltage-gated nanotrack.* Scientific reports, 2015. **5**: p. 11369.
30. Grigoriev, S., et al., *Helical spin structure of Mn 1− y Fe y Si under a magnetic field: Small angle neutron diffraction study.* Physical Review B, 2009. **79**(14): p. 144417.
31. Pappas, C., et al., *Chiral paramagnetic skyrmion-like phase in MnSi.* Physical review letters, 2009. **102**(19): p. 197202.
32. Zhang, S., et al., *Direct writing of room temperature and zero field skyrmion lattices by a scanning local magnetic field.* Applied Physics Letters, 2018. **112**(13): p. 132405.
33. Heinze, S., et al., *Spontaneous atomic-scale magnetic skyrmion lattice in two dimensions.* Nature Physics, 2011. **7**(9): p. 713.
34. Romming, N., et al., *Writing and deleting single magnetic skyrmions.* Science, 2013. **341**(6146): p. 636-639.
35. Schlenhoff, A., et al., *Magnetic nano-skyrmion lattice observed in a si-wafer-based multilayer system.* ACS nano, 2015. **9**(6): p. 5908-5912.
36. Everschor, K., *Current-induced dynamics of chiral magnetic structures: skyrmions, emergent electrodynamics and spin-transfer torques*. 2012, Universität zu Köln.
37. Nagaosa, N. and Y. Tokura, *Topological properties and dynamics of magnetic skyrmions.* Nature nanotechnology, 2013. **8**(12): p. 899.
38. Vansteenkiste, A., et al., *The design and verification of MuMax3.* AIP advances, 2014. **4**(10): p. 107133.
39. Gilbert, T.L., *A phenomenological theory of damping in ferromagnetic materials.* IEEE transactions on magnetics, 2004. **40**(6): p. 3443-3449.
40. Yoo, M.-W., V. Cros, and J.-V. Kim, *Current-driven skyrmion expulsion from magnetic nanostrips.* Physical Review B, 2017. **95**(18): p. 184423.
41. Zhang, S. and Z. Li, *Roles of nonequilibrium conduction electrons on the magnetization dynamics of ferromagnets.* Physical Review Letters, 2004. **93**(12): p. 127204.
42. Rohart, S. and A. Thiaville, *Skyrmion confinement in ultrathin film nanostructures in the presence of Dzyaloshinskii-Moriya interaction.* Physical Review B, 2013. **88**(18): p. 184422.
43. Heide, M., G. Bihlmayer, and S. Blügel, *Dzyaloshinskii-Moriya interaction accounting for the orientation of magnetic domains in ultrathin films: Fe/W (110).* Physical Review B, 2008. **78**(14): p. 140403.
44. Krishnia, S., et al., *Role of RKKY torque on domain wall motion in synthetic*

antiferromagnetic nanowires with opposite spin Hall angles. Scientific reports, 2017. **7**(1): p. 11715.
45. Thiaville, A., et al., *Dynamics of Dzyaloshinskii domain walls in ultrathin magnetic films.* EPL (Europhysics Letters), 2012. **100**(5): p. 57002.
46. Bogdanov, A. and A. Hubert, *Thermodynamically stable magnetic vortex states in magnetic crystals.* Journal of magnetism and magnetic materials, 1994. **138**(3): p. 255-269.
47. Bogdanov, A.N. and D. Yablonskii, *Thermodynamically stable "vortices" in magnetically ordered crystals. The mixed state of magnets.* Zh. Eksp. Teor. Fiz, 1989. **95**(1): p. 178.
48. Garcia, F., et al., *Exchange-biased spin valves with perpendicular magnetic anisotropy based on (Co/Pt) multilayers.* Journal of applied physics, 2003. **93**(10): p. 8397-8399.
49. Kalaycı, T., et al., *Tuning magnetic properties of non-collinear magnetization configuration in pt/[pt/co] 6/pt/co/pt multilayer structure.* Journal of Magnetism and Magnetic Materials, 2017. **436**: p. 11-16.
50. Zeper, W., et al., *Perpendicular magnetic anisotropy and magneto-optical Kerr effect of vapor-deposited Co/Pt-layered structures.* Journal of Applied Physics, 1989. **65**(12): p. 4971-4975.
51. Ummelen, F., et al., *Controlling the canted state in antiferromagnetically coupled magnetic bilayers close to the spin reorientation transition.* Applied Physics Letters, 2017. **110**(10): p. 102405.
52. Emori, S., et al., *Current-driven dynamics of chiral ferromagnetic domain walls.* Nature materials, 2013. **12**(7): p. 611.
53. 2019 30.04.2019]; Available from: http://www.semicore.com/what-is-sputtering.
54. Yamamoto, S. and I. Matsuda, *Measurement of the resonant magneto-optical Kerr effect using a free electron laser.* Applied Sciences, 2017. **7**(7): p. 662.
55. Lin, C.W., F.R.F. Fan, and A.J. Bard, *High resolution photoelectrochemical etching of n-GaAs with the scanning electrochemical and tunneling microscope.* J. Electrochem. Soc, 1987. **134**(4): p. 1038-1039.
56. Iwasaki, J., M. Mochizuki, and N. Nagaosa, *Current-induced skyrmion dynamics in constricted geometries.* Nature nanotechnology, 2013. **8**(10): p. 742.
57. Tchoe, Y. and J.H. Han, *Skyrmion generation by current.* Physical Review B, 2012. **85**(17): p. 174416.
58. Finazzi, M., et al., *Laser-induced magnetic nanostructures with tunable topological properties.* Physical review letters, 2013. **110**(17): p. 177205.
59. Büttner, F., et al., *Field-free deterministic ultrafast creation of magnetic skyrmions by spin–orbit torques.* Nature nanotechnology, 2017. **12**(11): p. 1040.
60. Ma, F., M. Ezawa, and Y. Zhou, *Microwave field frequency and current density modulated skyrmion-chain in nanotrack.* Scientific reports, 2015. **5**: p. 15154.
61. Jiang, W., et al., *Blowing magnetic skyrmion bubbles.* Science, 2015. **349**(6245): p. 283-286.
62. Zhou, Y. and M. Ezawa, *A reversible conversion between a skyrmion and a domain-wall pair in a junction geometry.* Nature communications, 2014. **5**: p. 4652.
63. Malozemoff, A. and J. Slonczewski, *Magnetic Domain Walls in Bubble Materials: Advances in Materials and Device Research*. Vol. 1. 2016: Academic press.
64. Büttner, F., I. Lemesh, and G.S. Beach, *Theory of isolated magnetic skyrmions: From fundamentals to room temperature applications.* Scientific reports, 2018. **8**(1): p. 4464.
65. Kwon, H., et al., *Effect of anisotropy and dipole interaction on long-range order magnetic structures generated by Dzyaloshinskii–Moriya interaction.* Journal of

Magnetism and Magnetic Materials, 2012. **324**(13): p. 2171-2176.
66. Tomasello, R., et al., *Origin of temperature and field dependence of magnetic skyrmion size in ultrathin nanodots.* Physical Review B, 2018. **97**(6): p. 060402.
67. Zhou, Y., et al., *Dynamically stabilized magnetic skyrmions.* Nature communications, 2015. **6**: p. 8193.
68. Bezvershenko, A.V., A.K. Kolezhuk, and B.A. Ivanov, *Stabilization of magnetic skyrmions by RKKY interactions.* Physical Review B, 2018. **97**(5): p. 054408.
69. Tomasello, R., et al., *Performance of synthetic antiferromagnetic racetrack memory: domain wall versus skyrmion.* Journal of Physics D: Applied Physics, 2017. **50**(32): p. 325302.
70. Zhang, X., Y. Zhou, and M. Ezawa, *Magnetic bilayer-skyrmions without skyrmion Hall effect.* Nature communications, 2016. **7**: p. 10293.